Journal of Sound and Vibration 644 (2026) 120053

Contents lists available at ScienceDirect

Journal of Sound and Vibration

journal homepage: www.elsevier.com/locate/jsvi

Global dynamical model reconstruction from local information in high-dimensional multi-stable systems

Jiawei Qian [a,b], Li Cheng [b,*], Xiuting Sun [a,*], Qian Lv [a], Jian Xu [a]

[a] School of Aerospace Engineering and Applied Mechanics, Tongji University, Shanghai, China
[b] Department of Mechanical Engineering, The Hong Kong Polytechnic University, Kowloon, Hong Kong, China

ARTICLE INFO

Keywords:
High-dimensional multi-stable structures
Model reconstruction
Global dynamics
Local dynamic responses
Coordinate coordination

ABSTRACT

High-dimensional multi-stable structures find broad engineering applications such as robotics and deployable structures. Accurate characterization of both intrawell and interwell dynamics is crucial for the design, optimization, and control of such structures. However, capturing their global dynamic features typically relies on large-amplitude dynamic responses, which are often impractical to obtain, especially in high-dimensional or highly damped systems. When the interwell separation in multi-stable systems significantly exceeds the amplitude of dynamic responses, traditional model reconstruction methods fail due to strong collinearity in the function library. To address this limitation, this paper presents a novel global model reconstruction method that employs local, small-amplitude dynamic responses. The proposed method is founded on a two-stage framework involving localized dynamics and coordinate coordination. First, multiple local dynamic models are constructed from small-amplitude dynamic responses, with each capturing the intrawell characteristics near a distinct equilibrium. Then, by applying the fundamental principle that the underlying global dynamics must have a unique mathematical form across all equilibria, a global dynamic model construction is performed. This process identifies the higher-order nonlinear terms that are absent in the local models due to their negligible effects on small-amplitude responses. These terms are subsequently integrated into a unified global dynamic model through coordinate transformation. Numerical and experimental verifications demonstrate the efficacy of the proposed method in reconstructing global models for multi-stable systems exhibiting multiple equilibria, asymmetric characteristics, and high Degrees-of-Freedom (DOFs). The results confirm the effectiveness and robustness of the method across varying amplitudes of dynamic response.

1. Introduction

Multi-stable structures hold significant application potential in engineering fields such as soft robotics [1,2], space-deployable structures [3,4], and mechanical computing [5,6], owing to their advantageous characteristics like fast response [7–9], low energy consumption [10–12], and rich deformation modes [13–15]. These applications require controlled switching between distinct configurations based on operational requirements. For instance, mechanical computing leverages specific configurations of mechanical metamaterials to conduct logic operations [16,17], whereas space-deployable structures must adopt a compact folded configuration

* Corresponding authors.
E-mail addresses: li.cheng@polyu.edu.hk (L. Cheng), 05mech_sunxiuting@tongji.edu.cn (X. Sun).

https://doi.org/10.1016/j.jsv.2026.120053
Received 24 April 2026; Received in revised form 6 July 2026; Accepted 7 August 2026
Available online 7 August 2026

Nomenclature

Abbreviation	*Full Term*
DOFs	Degrees-of-Freedom
NARX	Nonlinear Autoregressive with eXogenous inputs
RNN	Recurrent-Neural-Network
SINDy	Sparse Identification of Nonlinear Dynamics
S-DOF	Single-Degree-of-Freedom
M-DOF	Multi-Degree-of-Freedom
QRNN	Quasi-Recurrent Neural Network
NES	Nonlinear Energy Sink
GMC-SINDy	Generalized Method of Classical SINDy
LDSV	Large-Deformation-Small-Vibration
STLS	Sequential Threshold Least Squares
SNR	Signal-to-Noise Ratio
NRMSE	Normalized Root Mean Square Error
PSD	Power Spectral Density

during launch for vehicle compatibility, and then transition to a deployed configuration with an larger signal-receiving area to enhance transmission capability [18,19]. Accurate characterization of global dynamic behavior is therefore critical for operational stability and functional performance, a task that extends beyond the capability of traditional local linearization approximations. Consequently, a high-fidelity global dynamic model is indispensable for the design, analysis, and optimization of such high-dimensional multi-stable structures.

Data-driven approaches provide a feasible alternative to theoretical modeling for establishing global dynamical models of multi-stable systems. Without requiring prior explicit knowledge of the governing equations, these methods learn the system's nonlinear characteristics directly from response data. In recent years, various data-driven techniques have been proposed for reconstructing dynamical models of multi-stable systems, including Nonlinear Autoregressive with eXogenous inputs (NARX) [20,21], Recurrent-Neural-Network (RNN)-based methods [22,23], and sparse regression methods such as Sparse Identification of Nonlinear Dynamics (SINDy) [24,25]. Despite differences in model structure and implementation, the effectiveness of these approaches all relies on a common core assumption: the training data must encompass large-amplitude, global dynamical responses to fully capture the features of multiple attractors and their basin boundaries.

NARX modeling expresses the system output as a nonlinear function of past inputs and outputs, typically parameterized using basis functions such as polynomial expansions [26] or manifolds [27]. Accurate identification of the coefficients governing cross-attractor motion therefore requires training data containing large-amplitude transitions. Data confined to the vicinity of a single attractor yields models incapable of representing global behavior [28,29]. In contrast, RNN-based methods leverage their universal approximation capability to learn multi-stable dynamics implicitly from global responses in an end-to-end manner [30–32]. However, the strong expressive power of neural networks is contingent on response data sufficiently covering the basin-of-attraction space. Learning the boundaries and transition mechanisms between attractors necessitates a sufficiently large number of large-amplitude trajectories that cross these basins. Insufficient large-amplitude response data lead to overfitting, producing models that capture only local dynamics [33]. Sparse regression methods, exemplified by SINDy, aim to identify explicit governing equations directly from data. These methods assume the system dynamics can be sparsely represented by a few nonlinear terms, selected from a candidate library via compressed sensing or sparse optimization [34–36]. Despite their remarkable performance for monostable or low-dimensional multi-attractor systems, the success of these methods critically depends on the data trajectories traversing all important regions of the state space. Failure to meet this requirement can cause sparse regression to miss essential nonlinear terms, resulting in models that describe only locally stable equilibria.

However, acquiring continuous global dynamical response data from multi-stable systems is often infeasible. For low-dimensional systems, if dissipation is absent or sufficiently weak, appropriate periodic excitation can enable the system to surmount energy barriers, generating large-amplitude, cross-attractor motions [37–39]. Leveraging this principle, researchers have successfully applied various data-driven methods to Single-Degree-of-Freedom (S-DOF) and low-dimensional multi-stable systems. For example, Jin *et al.* proposed an Invertible Koopman Network for accurate attractor reconstruction in diverse multi-attractor systems [40], later extending its application to non-autonomous systems [41,42]. Yasuda *et al.* employed a Quasi-Recurrent Neural Network (QRNN) to achieve data-driven prediction of chaotic and periodic behaviors in a two-unit Kresling origami structure, revealing differentiated network response patterns to chaotic signals via hidden layer analysis [43]. Qian *et al.* introduced a data assembly principle to ensure dynamical ergodicity in training data for capturing global dynamic features of multi-stable systems, and established a bi-objective optimization framework for sparsification parameters to balance model accuracy and interpretability [44]. This method was first applied to reconstructing a bistable bio-inspired joint model and later extended to actuation optimization of deployable structures [45,46]. Jin *et al.* combined the restoring force surface method with the harmonic balance method for efficient, accurate, and interpretable structural health monitoring, validated on two-degree-of-freedom bistable Nonlinear Energy Sinks (NES) [47]. Significant challenges arise, however, with increased damping or system dimensionality. High damping dissipates the energy needed to cross energy barriers [48], making it difficult to obtain large-amplitude responses in S-DOF systems. Increasing excitation amplitude may only confine the system to small-amplitude oscillations within a single potential well [49]. The challenge intensifies with higher DOFs. For flexible structures comprising multiple serially connected multi-stable units, conventional periodic excitation can hardly induce simultaneous large-amplitude responses across all units [50]. Synchronous transitions demand prohibitively high input energy and precise phase coordination of excitations, which are often unattainable in experiments. A more common scenario is that only a few units exhibit large-amplitude responses while others undergoing small-amplitude vibrations. Further practical constraints for high-dimensional multi-stable systems make it exceptionally challenging to excite large-amplitude global dynamic responses simultaneously across all units.

A fundamental limitation of existing data-driven methods for high-dimensional multi-stable systems is thus their reliance on large-amplitude global dynamic response data, the acquisition of which is exceedingly difficult. To overcome this limitation, this paper introduces a novel global model reconstruction method capable of reconstructing the global dynamical model of a multi-stable system using only small-amplitude dynamical responses. The proposed method comprises two key stages. First, multiple local dynamic models are constructed from small-amplitude response data sampled in the vicinity of different stable equilibria. This captures the local dynamical features around each equilibrium while inherently eliminating the interference of large static deformations. Second, through coordinate coordination, the local information embedded within these models is leveraged to identify the higher-order nonlinear terms neglected in the first stage, thereby enabling the reconstruction of the system's global dynamic features. The effectiveness of the proposed method for high-dimensional multi-stable systems and its robustness with respect to the amplitude of the training data are validated through both numerical and experimental examples.

The remainder of the paper is structured as follows. Section 2 details the specific challenges to be addressed and outlines the procedure of the proposed global model reconstruction method. Section 3 validates the method's effectiveness via numerical examples. Section 4 demonstrates its application on an experimental prototype of a Multi-Degree-of-Freedom(M-DOF) multi-stable deployable structure; Section 5 provides concluding remarks.

2. Global model reconstruction method

2.1. Challenges for SINDy in multi-stable systems

For high-dimensional multi-stable systems, the primary challenge in model reconstruction lies in capturing not only the intrawell dynamic characteristics near multiple stable equilibria but also predicting the interwell dynamic behavior between them. To address this, data assembly principle is introduced within the classical SINDy framework to integrate dynamic response data from the vicinity of distinct equilibria, aiming to yield a model capable of capturing the system's global dynamics. However, the effectiveness of this enhanced SINDy approach is challenged when the amplitude of the dynamic response is significantly smaller than the static deformation between two equilibria. To illustrate the influence of the dynamic response amplitude on the method's effectiveness, a dynamic model reconstruction is performed for an M-DOF multi-stable system, as schematically shown in Fig. 1(a). Harmonic displacement excitations are applied at the base of the system under different configurations. The collected local dynamic response data for each cell are shown in Fig. 1(b). For different cells, the contrast between the intrawell dynamic response amplitude and the interwell separation is visually demonstrated within the restoring force curves plotted in Fig. 1(c). It can be observed that, as vibration transmits from the base to the distal end, the local dynamic response amplitude for each cell gradually decreases. Consequently, for the terminal cell (Cell

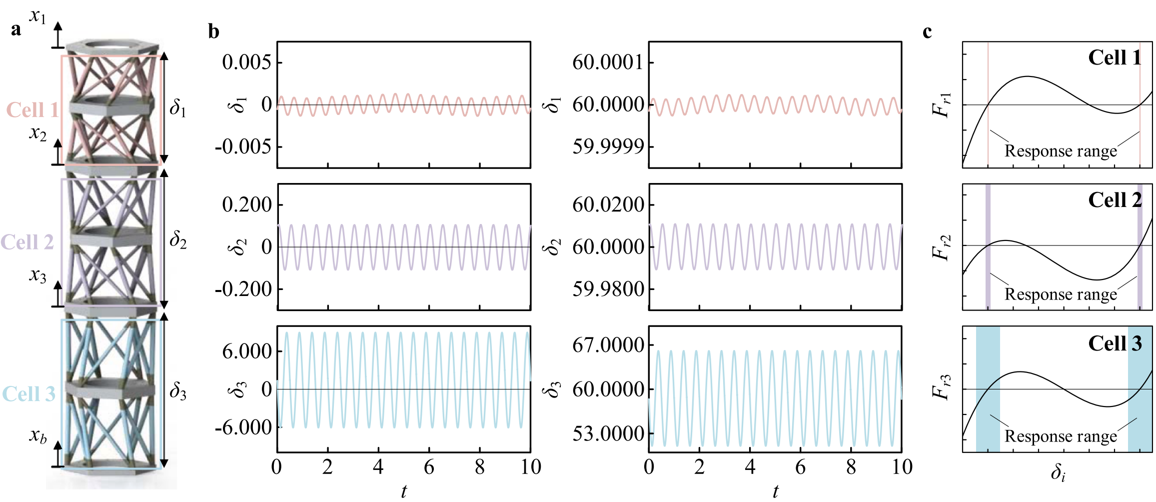

Fig. 1. Data collection process for a high-dimensional multi-stable deployable structure. **a** Schematic diagram and coordinate system definition for an M-DOF multi-stable structure. **b** Collected local dynamic response under harmonic displacement excitation applied at the base. **c** Range of local dynamic response for different cells.

1), the local dynamic response amplitude becomes significantly smaller than the static deformation between different equilibria, a scenario commonly seen in such high-dimensional complex dynamical systems

Using the local dynamic response data, the Generalized Method of Classical SINDy (GMC-SINDy) [44] is employed to reconstruct the dynamic model of the system in Fig. 1(a), with reconstruction results presented in Fig. 2. It can be observed that when the local dynamic response is relatively large (Cell 3), the GMC-SINDy method successfully captures the cell’s global restoring and damping force characteristics. However, as the local dynamic response amplitude decreases (Cells 1 and 2), the derived model can only capture the local restoring and damping properties, failing to predict global dynamic behavior. Furthermore, the effective range of the reconstruction model shrinks as the dynamic response amplitude decreases. Therefore, the global dynamic behavior of such multi-stable systems can be predicted by the reconstruction model only when the dynamic response amplitude in the training data exceeds a certain threshold (as in Cell 3). Fundamentally, the failure of GMC-SINDy originates from the significant magnitude difference between static deformation and dynamic response. This difference results in severe collinearity within the restoring force terms of the library function matrix constructed via the data assembly principle, leading to the failure in achieving accurate coefficient identification. In Appendix A, via Fourier expansion of the response data, we demonstrate why the Large-Deformation-Small-Vibration (LDSV) phenomenon leads to strong collinearity in the library function matrix.

2.2. Global model reconstruction via localized dynamics and coordinate coordination

We hereby propose a global model reconstruction method based on localized dynamics and coordinate coordination, aiming to achieve global dynamic prediction of multi-stable systems using only small-amplitude dynamic responses. The method primarily consists of two stages: local dynamic model analysis and global dynamic model construction, as summarized in the flowchart (Fig. 3). In the local dynamic model analysis stage, multiple local dynamic models are established using small-amplitude vibration data sampled near different equilibria. Each local model is designed to capture the intrawell dynamic characteristics in the vicinity of its corresponding equilibrium. Without simultaneously considering data from multiple equilibria, the dominant static deformation components can be eliminated through coordinate transformation during the construction of each local model, thereby avoiding the strong collinearity issues inherent to the LDSV phenomenon. Subsequently, in the second global dynamic model construction stage, the global dynamic model is inferred from the multiple local models by leveraging the fundamental principle that the system's underlying global dynamics must have a unique mathematical form and consistent coefficients across all equilibria.

a

Cell 1

Governing equations: $\ddot{q}_1 + \sum_{i=0}^{5} A_{1i}\delta_1^{\,i}\dot{\delta}_1 + \sum_{i=0}^{5} B_{1i}\delta_1^{\,i} = 0$

A_{10}	1.96×10^{-3}	A_{14}	1.58×10^{8}	B_{10}	0	B_{13}	6.82×10^{3}
A_{11}	-4.05	A_{15}	-2.76×10^{9}	B_{11}	9.66×10^{-3}	B_{14}	-1.80×10^{5}
A_{12}	-2.99×10^{6}	A_{16}	1.61×10^{10}	B_{12}	-57.69	B_{15}	1.36×10^{6}

b

Cell 2

Governing equations: $\ddot{q}_2 + \sum_{i=0}^{5} A_{2i}\delta_2^{\,i}\dot{\delta}_2 + \sum_{i=0}^{5} B_{2i}\delta_2^{\,i} = 0$

A_{20}	1.20×10^{-3}	A_{24}	-3.58×10^{3}	B_{20}	0	B_{23}	32.36
A_{21}	0	A_{25}	-5.70×10^{5}	B_{21}	3.62×10^{-3}	B_{24}	-918.42
A_{22}	826.35	A_{26}	6.66×10^{6}	B_{22}	-0.33	B_{25}	7.58×10^{3}

c

Cell 3

Governing equations: $\ddot{q}_3 + \sum_{i=0}^{5} A_{3i}\delta_3^{\,i}\dot{\delta}_3 + \sum_{i=0}^{5} B_{3i}\delta_3^{\,i} = 0$

A_{30}	1.70×10^{-3}	A_{34}	0	B_{30}	7.18×10^{-3}	B_{33}	0
A_{31}	0	A_{35}	0	B_{31}	-0.36	B_{34}	0
A_{32}	0	A_{36}	0	B_{32}	3.99	B_{35}	0

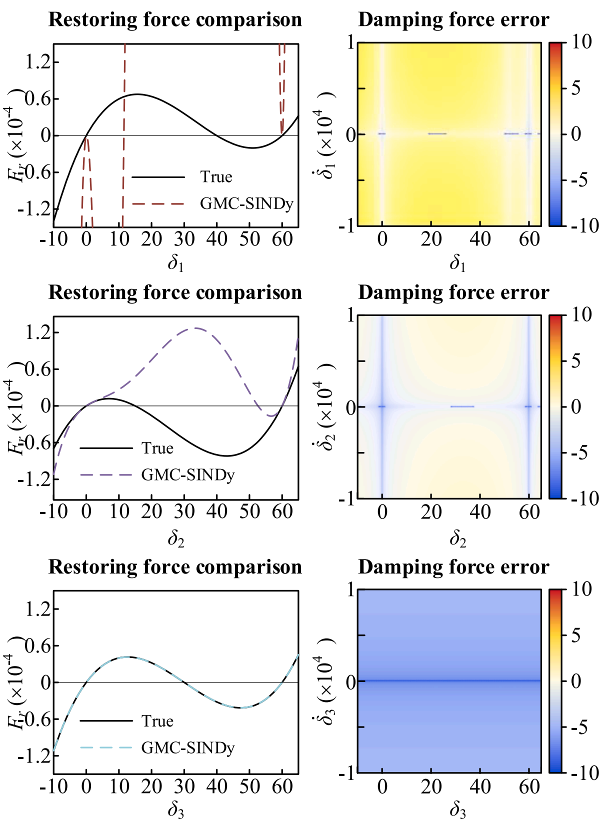

Fig. 2. Effect of local dynamic response amplitude on the validity of the GMC-SINDy method. **a** Cell 1. **b** Cell 2. **c** Cell 3.

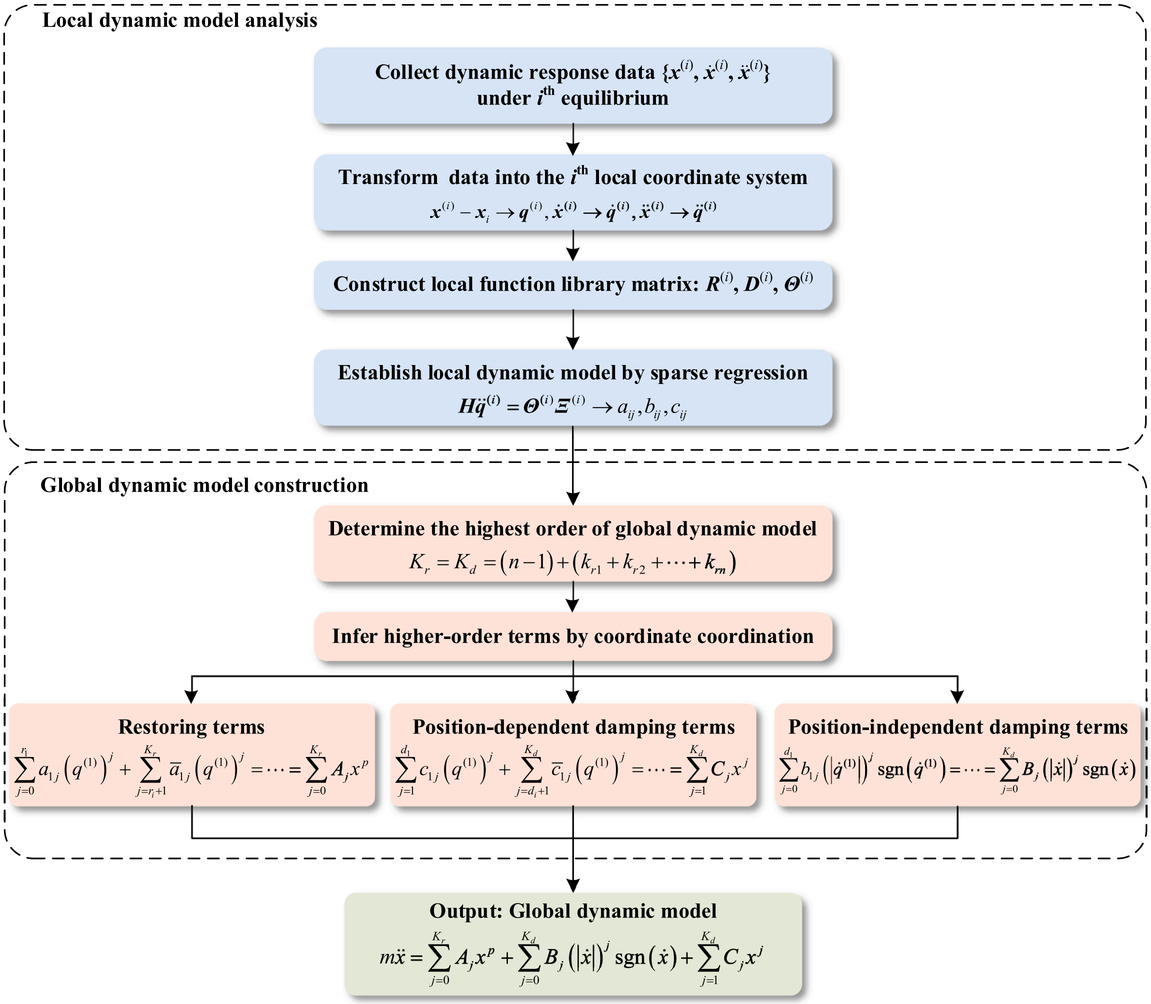

Fig. 3. Algorithm flowchart of the proposed global model reconstruction method based on localized dynamics and coordinate coordination.

2.2.1. Local dynamic model analysis

Considering the M-DOF multi-stable system shown in Fig. 1(a), the global dynamic model in the global coordinate system can be expressed as

$$\mathbf{M}\ddot{\mathbf{x}} + \mathbf{F}_d(\dot{\mathbf{x}}, \mathbf{x}) + \mathbf{F}_r(\mathbf{x}) = \mathbf{f}(t), \tag{1}$$

where $\mathbf{x}$, $\dot{\mathbf{x}}$, $\ddot{\mathbf{x}}$ are the generalized displacement, velocity, and acceleration vectors of the system, respectively; $\mathbf{M}$ is the mass matrix, $\mathbf{F}_d$ and $\mathbf{F}_r$ represent the damping force and restoring force vectors. The system possesses n equilibria, denoted as $\mathbf{x}_1, \mathbf{x}_2, \ldots, \mathbf{x}_n$. First, the dynamic response data near each equilibrium, denoted as $\{\mathbf{x}^{(i)}, \dot{\mathbf{x}}^{(i)}, \ddot{\mathbf{x}}^{(i)}\}$, are collected in the global coordinate system, where the superscript i corresponds to the i^{th} equilibrium. The acquired generalized displacement data $\mathbf{x}^{(i)}$ contain two distinct components: $\mathbf{x}_i$, representing the static equilibrium deformation, and $\mathbf{x}^{(i)} - \mathbf{x}_i$, representing the intrawell vibration near the equilibrium. As demonstrated in Section 2.1, when static equilibrium deformation $\mathbf{x}_i$ is significantly larger than the amplitude of intrawell vibration $\mathbf{x}^{(i)} - \mathbf{x}_i$, severe collinearity is induced within the restoring force terms of the library function matrix, leading to the failure of GMC-SINDy. Consequently, during the construction of the local dynamic model corresponding to the i^{th} equilibrium, the following coordinate transformation is employed to eliminate the influence of the static equilibrium deformation:

$$\mathbf{q}^{(i)} = \mathbf{x}^{(i)} - \mathbf{x}_i, \tag{2}$$

where $\mathbf{q}^{(i)}$ is the generalized displacement in the i^{th} local coordinate system. The corresponding generalized velocity and acceleration are

$$\dot{\mathbf{q}}^{(i)} = \dot{\mathbf{x}}^{(i)}, \tag{3}$$

$$\ddot{\mathbf{q}}^{(i)} = \ddot{\mathbf{x}}^{(i)}. \tag{4}$$

Subsequently, the library function matrix $\mathbf{\Theta}^{(i)}$, consisting of candidate nonlinear functions of $\mathbf{q}^{(i)}$ and $\dot{\mathbf{q}}^{(i)}$, is constructed. This library function matrix can be expressed as

$$\mathbf{\Theta}^{(i)} = \begin{bmatrix} | & | \\ \mathbf{R}^{(i)} & \mathbf{D}^{(i)} \\ | & | \end{bmatrix}, \tag{5}$$

where $\mathbf{R}^{(i)}$ and $\mathbf{D}^{(i)}$ are vectors of candidate functions representing restoring and damping terms, respectively. In this work, polynomial functions are selected as candidate functions to express both restoring and damping terms. The essential requirement for candidate function is that higher-order basis project onto lower-order basis under coordinate transformation Eq. (2). Other basis functions, such as Legendre and Chebyshev polynomials, also satisfy this property and are compatible with our framework. The restoring force candidate matrix $\mathbf{R}^{(i)}$ can be expressed as

$$\mathbf{R}^{(i)} = \begin{bmatrix} | & | & | & & | \\ 1 & \mathbf{q}^{(i)} & \left(\mathbf{q}^{(i)}\right)^2 & \cdots & \left(\mathbf{q}^{(i)}\right)^r \\ | & | & | & & | \end{bmatrix}, \tag{6}$$

where r is the highest order of restoring force candidate functions. For damping terms, both position-independent and position-dependent damping are considered. The damping force candidate matrix $\mathbf{D}^{(i)}$ is formulated as

$$\mathbf{D}^{(i)} = \begin{bmatrix} | & | & & | & | & | & & | \\ \mathrm{sgn}\left(\dot{\mathbf{q}}^{(i)}\right) & \left|\dot{\mathbf{q}}^{(i)}\right|\mathrm{sgn}\left(\dot{\mathbf{q}}^{(i)}\right) & \cdots & \left|\dot{\mathbf{q}}^{(i)}\right|^d\mathrm{sgn}\left(\dot{\mathbf{q}}^{(i)}\right) & \left|\mathbf{q}^{(i)}\right|\dot{\mathbf{q}}^{(i)} & \left|\mathbf{q}^{(i)}\right|^2\dot{\mathbf{q}}^{(i)} & \cdots & \left|\mathbf{q}^{(i)}\right|^d\dot{\mathbf{q}}^{(i)} \\ | & | & & | & | & | & & | \end{bmatrix}, \tag{7}$$

where d is the highest order of the damping force candidate functions. After constructing the library function matrix, the following sparse regression formulation is established to identify the local model

$$\mathbf{H}\ddot{\mathbf{q}}^{(i)} = \mathbf{\Theta}^{(i)}\mathbf{\Xi}^{(i)}, \tag{8}$$

where $\mathbf{\Xi}^{(i)}$ is a sparse coefficient matrix determining which candidate functions are active in the i^{th} local dynamic model. $\mathbf{H}$ is a coordinate transformation matrix to decouple the equations of motion for different degrees of freedom (i.e., cells), expressed as

$$\mathbf{H} = \begin{pmatrix} m_1 & 0 & 0 & \cdots & 0 \\ m_1 & m_2 & 0 & \cdots & 0 \\ m_1 & m_2 & \ddots & & \vdots \\ \vdots & \vdots & & m_{n-1} & 0 \\ m_1 & m_2 & \cdots & m_{n-1} & m_n \end{pmatrix}. \tag{9}$$

To solve the sparse regression problem in Eq. (8), different sparse regression methods can be applied. In this work, we adopt the Sequential Threshold Least Squares (STLS) algorithm [51,52], which is the standard solver in the original SINDy framework [34], offering superior computational efficiency and a physically intuitive sparsification parameter compared to LASSO or Ridge. Once the sparse coefficient matrix $\mathbf{\Xi}^{(i)}$ is determined, the local dynamic model describing the intrawell vibration characteristics of the i^{th} equilibrium is constructed.

2.2.2. Global dynamic model construction

During the construction of the local dynamic models, higher-order terms that exert negligible influence on the small-amplitude intrawell response are omitted. Consequently, these local models alone cannot accurately characterize the global dynamic behavior of the system. By taking these neglected higher-order nonlinear terms into account, and leveraging the principle that the true global dynamics must have a unique form, the local models identified above can be related via coordinate coordination to recover a unified global model with consistent coefficients. Utilizing this property, the global dynamic model can be inferred from the set of local dynamic models. Taking an S-DOF system as an example, the obtained local dynamic model for the i^{th} equilibrium can be expressed as

$$\ddot{q}^{(i)} = \sum_{j=0}^{r_i} a_{ij}\left(q^{(i)}\right)^j + \sum_{j=0}^{d_i} b_{ij}\left(\left|\dot{q}^{(i)}\right|\right)^j \mathrm{sgn}\left(\dot{q}^{(i)}\right) + \left(\sum_{j=1}^{d_i} c_{ij}\left(q^{(i)}\right)^j\right)\dot{q}^{(i)}, i = 1, \cdots, n, \tag{10}$$

where r_i and d_i are the identified highest orders of the restoring and damping force terms, respectively; n the number of equilibria; a_{ij}, b_{ij} and c_{ij} the identified coefficients of restoring, position-independent damping and position-dependent damping terms, respectively. As noted in Section 2.2.1, when the intrawell vibration amplitude is small, the influence of certain higher-order terms in the dynamic model is minor, and thus they may not be identified in the local dynamic model. By considering these potentially neglected higher-order terms, the local dynamic model in Eq. (10) can be rewritten in a complete form as

$$\ddot{q}^{(i)} = \sum_{j=0}^{r_i} a_{ij}\left(q^{(i)}\right)^j + \sum_{j=r_i+1}^{K_r} \overline{a}_{ij}\left(q^{(i)}\right)^j + \sum_{j=0}^{d_i} b_{ij}\left(\left|\dot{q}^{(i)}\right|\right)^j \mathrm{sgn}\left(\dot{q}^{(i)}\right) + \left(\sum_{j=1}^{d_i} c_{ij}\left(q^{(i)}\right)^j + \sum_{j=d_i+1}^{K_d} \overline{c}_{ij}\left(q^{(i)}\right)^j\right)\dot{q}^{(i)}, \tag{11}$$

where K_r and K_d are the unknown highest order of the global restoring and position-dependent damping terms; The coefficients for higher orders $\overline{a}_{ij}$ and $\overline{c}_{ij}$ are unknown in the local model identification stage and to be determined via global dynamic model construction.

Next, according to coordinate coordination, these coefficients for higher orders are inferred. The prevailing idea underpinning the coordinate coordination is that the physical system has a unique global dynamic form. When the local models as Eq. (11) are transformed back to the global coordinate x through $q^{(i)} = x - x_i$, this yields the following coordinate coordination conditions for the restoring, position-independent damping, and position-dependent damping terms, respectively, as

$$\sum_{j=0}^{r_1} a_{1j}\left(q^{(1)}\right)^j + \sum_{j=r_i+1}^{K_r} \overline{a}_{1j}\left(q^{(1)}\right)^j = \cdots = \sum_{j=0}^{r_n} a_{1j}\left(q^{(n)}\right)^j + \sum_{j=r_i+1}^{K_r} \overline{a}_{1j}\left(q^{(n)}\right)^j = \sum_{j=0}^{K_r} A_j x^p, \tag{12}$$

$$\sum_{j=0}^{d_1} b_{1j}\left(\left|\dot{q}^{(1)}\right|\right)^j \mathrm{sgn}\left(\dot{q}^{(1)}\right) = \cdots = \sum_{j=0}^{d_n} b_{nj}\left(\left|\dot{q}^{(n)}\right|\right)^j \mathrm{sgn}\left(\dot{q}^{(n)}\right) = \sum_{j=0}^{K_d} B_j\left(|\dot{x}|\right)^j \mathrm{sgn}(\dot{x}), \tag{13}$$

$$\sum_{j=1}^{d_1} c_{1j}\left(q^{(1)}\right)^j + \sum_{j=d_i+1}^{K_d} \overline{c}_{1j}\left(q^{(1)}\right)^j = \cdots = \sum_{j=1}^{d_n} c_{nj}\left(q^{(n)}\right)^j + \sum_{j=d_i+1}^{K_d} \overline{c}_{nj}\left(q^{(n)}\right)^j = \sum_{j=1}^{K_d} C_j x^j, \tag{14}$$

where A_j, B_j and C_j are the unknown coefficients of the global dynamic model's restoring, position-independent damping, position-dependent damping force terms to be determined. The goal of the global dynamic model construction is to infer the global coefficients A_j, B_j and C_j from the known local coefficients a_{ij}, b_{ij} and c_{ij}.

Firstly, the construction of restoring terms, constrained by Eq. (12), is considered. Equation (12) can be rewritten in the following matrix form for all n equilibria as

$$\begin{bmatrix} \mathbf{U}_1 & -\mathbf{U}_2 & 0 & \cdots & 0 \\ \mathbf{U}_1 & 0 & -\mathbf{U}_3 & \cdots & 0 \\ \vdots & \vdots & \vdots & & \vdots \\ \mathbf{U}_1 & 0 & 0 & \cdots & -\mathbf{U}_n \end{bmatrix} \begin{bmatrix} \overline{\mathbf{a}}_1 \\ \overline{\mathbf{a}}_2 \\ \vdots \\ \overline{\mathbf{a}}_n \end{bmatrix} = \begin{bmatrix} \mathbf{V}_1 & -\mathbf{V}_2 & 0 & \cdots & 0 \\ \mathbf{V}_1 & 0 & -\mathbf{V}_3 & \cdots & 0 \\ \vdots & \vdots & \vdots & & \vdots \\ \mathbf{V}_1 & 0 & 0 & \cdots & -\mathbf{V}_n \end{bmatrix} \begin{bmatrix} \mathbf{a}_1 \\ \mathbf{a}_2 \\ \vdots \\ \mathbf{a}_n \end{bmatrix}, \tag{15}$$

where $\overline{\mathbf{a}}_i = \left[\overline{a}_{r_i+1} \quad \cdots \quad \overline{a}_{K_r}\right]^{\mathrm{T}}$, $\mathbf{a}_i = \left[a_1 \quad \cdots \quad a_{r_i}\right]^{\mathrm{T}}$ are vectors of identified and unknown local restoring force coefficients, respectively. $\mathbf{U}_i$ and $\mathbf{V}_i$ are block matrices constructed from the equilibrium position x_i, with the i^{th} blocks, expressed as

$$\mathbf{U}_i = \begin{bmatrix} (-x_i)^{r_i+1} & (-x_i)^{r_i+2} & \cdots & (-x_i)^{K_r} \\ \mathrm{C}^1_{r_i+1}(-x_i)^{r_i} & \mathrm{C}^1_{r_i+2}(-x_i)^{r_i+1} & \cdots & \mathrm{C}^1_{K_r}(-x_i)^{K_r-1} \\ \mathrm{C}^2_{r_i+1}(-x_i)^{r_i-1} & \mathrm{C}^2_{r_i+2}(-x_i)^{r_i} & \cdots & \mathrm{C}^2_{K_r}(-x_i)^{K_r-2} \\ \vdots & \vdots & & \vdots \\ 0 & 0 & \cdots & \mathrm{C}^{K_r}_{K_r} \end{bmatrix}, \tag{16}$$

$$\mathbf{V}_i = \begin{bmatrix} 1 & (-x_i)^1 & (-x_i)^2 & \cdots & (-x_i)^{r_i} \\ 0 & 1 & \mathrm{C}^1_2(-x_i)^1 & \cdots & \mathrm{C}^1_{r_i}(-x_i)^{r_i-1} \\ 0 & 0 & 1 & \cdots & \mathrm{C}^2_{r_i}(-x_i)^{r_i-2} \\ \vdots & \vdots & \vdots & & \vdots \\ 0 & 0 & 0 & \cdots & 0 \end{bmatrix}. \tag{17}$$

In Eq. (15), the unknown coefficients of the higher-order terms $\overline{\mathbf{a}}_i$ are on the left-hand side, while the known local coefficients $\mathbf{a}_i$ are on the right. This constitutes a system of linear equations for the unknowns. The solvability and uniqueness of its solutions for the unknown coefficients depend on the chosen highest order K_r. Since the underlying global dynamic model of a multi-stable system must be unique, the equations must be constructed to yield a unique solution. Consequently, the correct K_r is determined as the minimum value for which the linear system in Eq. (15) has a unique solution. The equivalent condition is given as

$$K_r = (n-1) + (k_{r1} + k_{r2} + \cdots + k_{rn}). \tag{18}$$

Once K_r is determined, all unknown coefficients can be obtained by solving Eq. (15). Thus, the restoring force expression in the global coordinate system can be further derived through Eq. (12).

Next, the construction for the position-dependent damping terms, constrained by Eq. (14), is considered. Similarly, Eq. (14) can be rewritten in a matrix form as

$$\begin{bmatrix} \mathbf{U}_1 & -\mathbf{U}_2 & 0 & \cdots & 0 \\ \mathbf{U}_1 & 0 & -\mathbf{U}_3 & \cdots & 0 \\ \vdots & \vdots & \vdots & & \vdots \\ \mathbf{U}_1 & 0 & 0 & \cdots & -\mathbf{U}_n \end{bmatrix} \begin{bmatrix} \bar{\mathbf{c}}_1 \\ \bar{\mathbf{c}}_2 \\ \vdots \\ \bar{\mathbf{c}}_n \end{bmatrix} = \begin{bmatrix} \mathbf{V}_1 & -\mathbf{V}_2 & 0 & \cdots & 0 \\ \mathbf{V}_1 & 0 & -\mathbf{V}_3 & \cdots & 0 \\ \vdots & \vdots & \vdots & & \vdots \\ \mathbf{V}_1 & 0 & 0 & \cdots & -\mathbf{V}_n \end{bmatrix} \begin{bmatrix} \mathbf{c}_1 \\ \mathbf{c}_2 \\ \vdots \\ \mathbf{c}_n \end{bmatrix}, \tag{19}$$

which is analogous to Eq. (15). Therefore, the highest order K_d for the position-dependent damping terms can be determined by a condition analogous to Eq. (18), as

$$K_d = (n-1) + (k_{d1} + k_{d2} + \cdots + k_{dn}). \tag{20}$$

After K_d is determined, the unknown coefficients for the position-dependent damping terms are obtained by solving Eq. (19).

Finally, the construction of position-independent damping terms, constrained by Eq. (13), is addressed. Since the position-independent damping term is a function of velocity only, its functional form and coefficients should be identical across all local models when expressed in the global velocity coordinate. Consequently, the global coefficients B_j can be directly estimated as the average of the corresponding identified local coefficients b_{ij} from all n equilibria as

$$B_j = \frac{1}{n}\sum_{i=1}^{n} b_{ij}, j = 1, \ldots, K_d. \tag{21}$$

After obtaining all global coefficients, the global dynamic model, capable of capturing both intrawell and interwell dynamic

Algorithm 1
Global model reconstruction method.

Function GMR ($\mathbf{X}$, $\dot{\mathbf{X}}$, $\ddot{\mathbf{X}}$, r, d, λ)
Input:
▷ $\mathbf{X} = \{\mathbf{x}^{(1)}, \ldots, \mathbf{x}^{(n)}\}$: Generalized displacement matrix
▷ $\dot{\mathbf{X}} = \{\dot{\mathbf{x}}^{(1)}, \ldots, \dot{\mathbf{x}}^{(n)}\}$: Generalized velocity matrix
▷ $\ddot{\mathrm{X}} = \left\{\ddot{\mathrm{x}}^{(1)}, \ldots, \ddot{\mathrm{x}}^{(n)}\right\}$: Generalized acceleration matrix
▷ r: Highest order of restoring force candidate functions
▷ d: Highest order of damping force candidate functions
▷ λ: Sparsification parameter
Output:
▷ $\mathbf{A}$: Restoring coefficient matrix in global coordinate system
▷ $\mathbf{B}$: Position-independent damping coefficient matrix in global coordinate system
▷ $\mathbf{C}$: Position-dependent damping coefficient matrix in global coordinate system
// Stage 1: Local dynamic model analysis
for $i \leftarrow 1$ to n **do**

// Step 1.1: Coordinate transformation: Global to local
$\mathbf{x}_i \leftarrow$ mean($\mathbf{x}^{(i)}$, 2) // Compute i^{th} equilibrium position in the global coordinate system
$\mathbf{q}^{(i)} \leftarrow \mathbf{x}^{(i)} - \mathbf{x}_i$, $\dot{\mathbf{q}}^{(i)} \leftarrow \dot{\mathbf{x}}^{(i)}$, $\ddot{\mathrm{q}}^{(i)} \leftarrow \ddot{\mathrm{x}}^{(i)}$ // Coordinate transformation

// Step 1.2:Local feature matrix construction
$\mathbf{H}^{(i)} \leftarrow$ Eq. (9) // Decouple equations of motion for different degrees of freedom
$\mathbf{R}^{(i)} \leftarrow$ Eq. (6), $\mathbf{D}^{(i)} \leftarrow$ Eq. (7), $\mathbf{\Theta}^{(i)} \leftarrow$ Eq. (5) // Local library function matrix construction

// Step 1.3: Sparse identification for local dynamic model
$\mathbf{\Xi}^{(i)} \leftarrow \mathrm{argmin}((||\mathbf{H}^{(i)}\ddot{\mathrm{q}}^{(i)} - \mathbf{\Theta}^{(i)}\mathbf{\Xi}^{(i)}||_2)^2 + \lambda||\mathbf{\Xi}^{(i)}||_0)$ // Sparse identification by STLS

// Step 1.4: Decompose stacked local coefficients into physical vectors
$\mathbf{a}_i \leftarrow \mathbf{\Xi}^{(i)}[1: r]$, $\mathbf{b}_i \leftarrow \mathbf{\Xi}^{(i)}[r+1: r+d]$, $\mathbf{c}_i \leftarrow \mathbf{\Xi}^{(i)}[r+d+1: r+2d]$
end for

// Stage 2: Global dynamic model construction
for $q \leftarrow 1$ to n **do**

// Step 2.1: Global model order determination
$K_r \leftarrow$ Eq. (18) using $\mathbf{a}_i$ // Restoring order determination
$K_d \leftarrow$ Eq. (20) using $\mathbf{c}_i$ // Damping order determination

// Step 2.2: Coordinate coordination conditions
$\mathbf{U}_i \leftarrow$ Eq. (16) using K_r, $\mathbf{x}_i$; $\mathbf{V}_i \leftarrow$ Eq. (17) using K_d, $\mathbf{x}_i$ // Coordinate coordination matrices construction
$\bar{\mathbf{a}}_i \leftarrow$ Eq. (15) using $\mathbf{U}_i$, $\mathbf{V}_i$, $\mathbf{a}_i$ // Coordinate coordination conditions for higher-order restoring terms
$\bar{\mathbf{c}}_i \leftarrow$ Eq. (19) using $\mathbf{U}_i$, $\mathbf{V}_i$, $\mathbf{c}_i$ // Coordinate coordination conditions for higher-order damping terms

// Step 2.3: Mapping of dynamic model coefficients: from local to global coordinate systems
$\mathbf{A}_q \leftarrow$ Eq. (12), $\mathbf{B}_q \leftarrow$ Eq. (21), $\mathbf{C}_q \leftarrow$ Eq. (14) // Global model coefficients derivation
end for

behaviors of the multi-stable system, is established. The overall reconstruction process is summarized in Algorithm 1 and the flowchart of Fig. 3.

2.3. A baseline example

To further substantiate the process and demonstrate the effectiveness of the proposed method, global model reconstruction is performed for an S-DOF bistable bionic joint [44]. Its schematic diagram and governing equation are shown in Fig. 4(a), where F_r and F_d represent the restoring and damping forces, respectively. A pair of balance springs is symmetrically connected to both sides of the bistable bionic joint, and a torsion spring is connected at the center of hinge joint. These elastic components constitute the bistable restoring force characteristics of the joint. Energy dissipation in the bistable bionic joint stems from two sources: one from the friction at the joint, typical of position-independent damping force; and the other from the balance springs themselves possessing viscoelastic damping properties and representative of position-dependent damping force. The expression for the restoring force F_r and its force-displacement relationship are presented in Fig. 4(b), revealing two stable equilibria S1 and S2. Two distinct damping models are

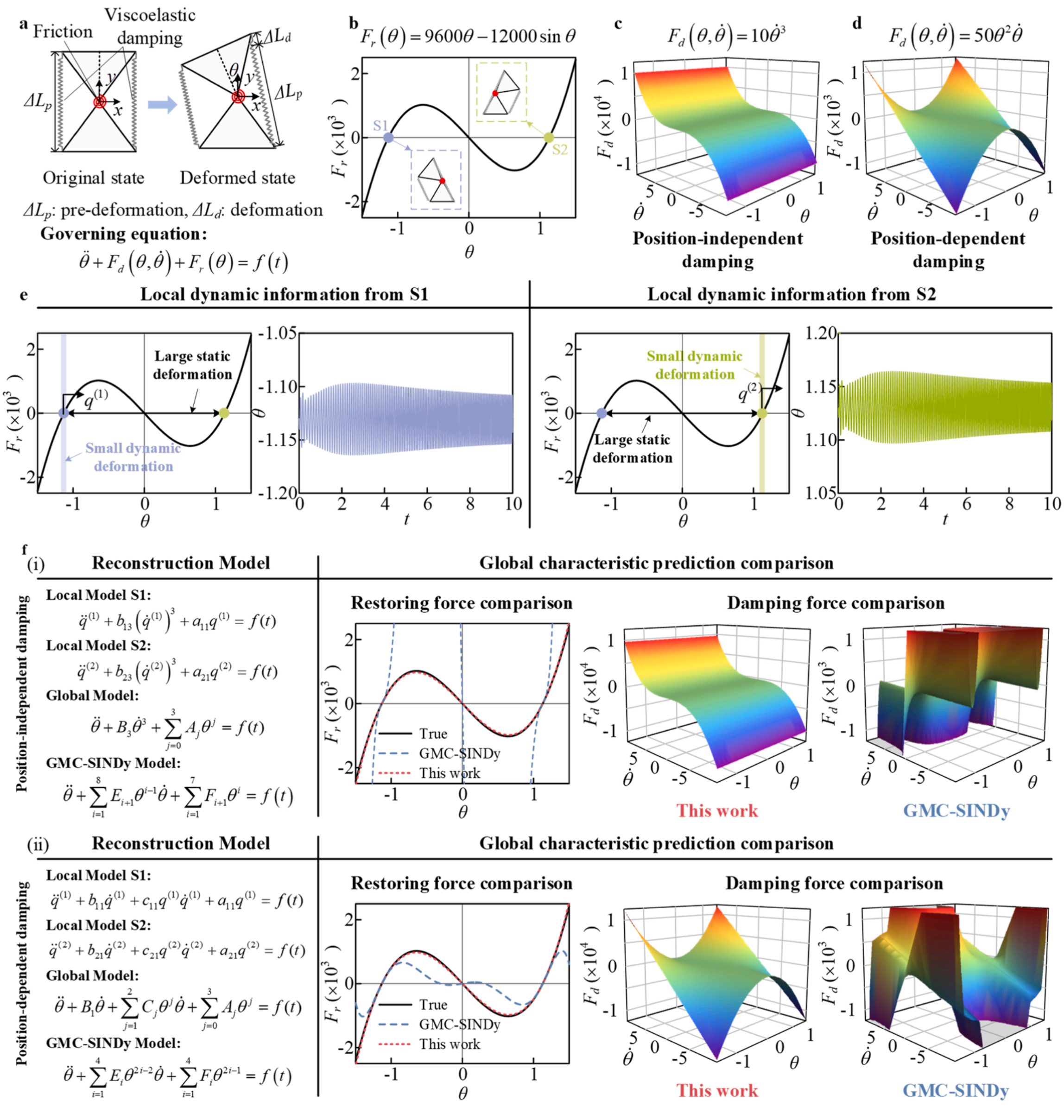

Fig. 4. Global model reconstruction of a bistable bionic joint. (a) Mechanical model and governing equation. (b) Restoring force-displacement relationship. (c, d) Expressions and damping force surfaces for the position-independent and position-dependent damping models. (e) Intrawell dynamic response data collected near different equilibria. (f) Comparison of reconstructed models and global characteristic predictions.

considered. The first one is a position-independent cubic nonlinear damping model, and the second a position-dependent damping model where the damping force is proportional to the square of the displacement. Their mathematical expressions and the corresponding damping force variations are shown in Figs. 4(c) and (d), respectively. Small-amplitude sweep torsional displacement excitations are to acquire intrawell dynamic response data near the equilibria S1 and S2, as shown in Fig. 4(e). Figure 4(e) also superimposes the range of these dynamic responses onto the global restoring force curve. It can be observed that the amplitude of the dynamic responses near each equilibrium is significantly smaller than the interwell separation, confirming the LDSV phenomenon. Using the dynamic response data from Fig. 4(e), the global dynamic model is reconstructed using both the GMC-SINDy method and the proposed method. In the proposed global model reconstruction method, polynomial orders of the restoring and damping force candidate matrices are set to $r = 5$ and $d = 5$, respectively, to construct the local dynamic models near the two equilibria, which ultimately reconstructs a global model with terms up to 11th order. For comparison, GMC-SINDy uses 7th-order global libraries for both forces ($r = 7$ and $d = 7$). This highlights the inherent advantage of our method: a lower-order library is suffcient to capture the local dynamical behavior near a specific equilibrium, whereas a higher-order representation is required to describe the global dynamics. Consequently, our strategy effectively circumvents severe collinearity issues that typically plague high-order global library matrices in GMC-SINDy. The reconstruction results for the first and second damping models are presented in Fig. 4f(i) and (ii), respectively, and the numerical coefficients of the identified local models and global models are listed in Tables B1 and B2, Appendix B. These subfigures compare the restoring force and damping force models obtained via GMC-SINDy and the proposed method against the true global characteristics. From Fig. 4(f), it is observed that for the restoring force, GMC-SINDy only offer faithful description near the equilibria, exhibiting significant errors in the interwell region. Conversely, the model obtained by the proposed method achieves precise characterization of the global restoring force features. This is attributed to the accurate identification of the local stiffness near each equilibrium by the two respective local models. For the damping force, the proposed method accurately identifies both damping

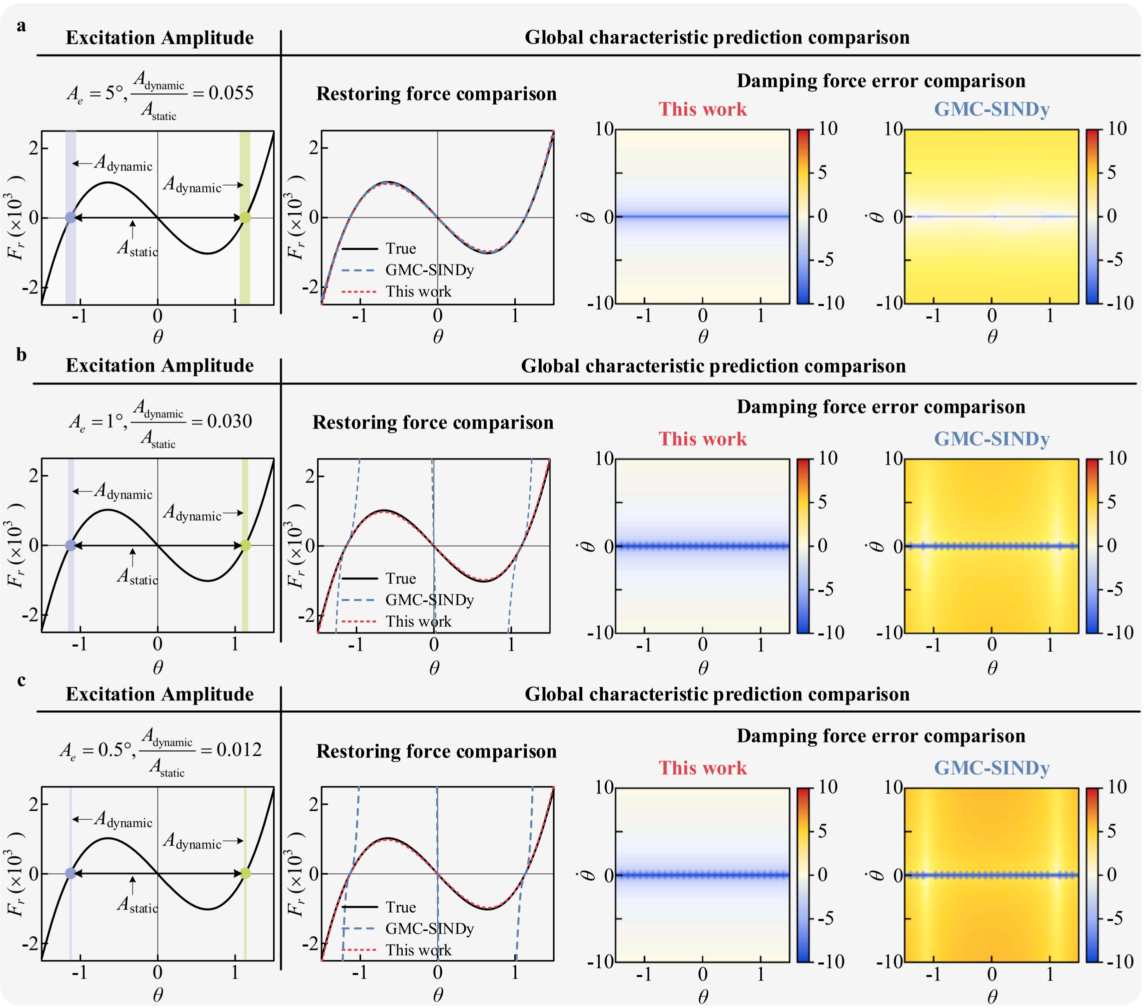

Fig. 5. Global model reconstruction results for position-independent damping model under different excitation amplitudes A_e: (a) $A_e = 5°$. (b) $A_e = 1°$. (c) $A_e = 0.5°$.

models, whereas GMC-SINDy fails to identify either. This demonstrates that although the strong collinearity in the GMC-SINDy library is primarily induced by displacement-related terms, it compromises the reconstruction of both restoring and damping forces.

Subsequently, to investigate the sensitivity of the proposed method to the dynamic response amplitude, model reconstruction is performed using data of varying amplitudes alongside comparisons with the GMC-SINDy method. Figure 5 presents the GMC-SINDy result and that from the proposed method for the position-independent damping model under different excitation amplitudes. The following damping force error metric is defined to quantify the discrepancy between the true and reconstruction forces as

$$e_d = \log_{10}|F_d - \overline{F}_d|, \tag{22}$$

where F_d and $\overline{F}_d$ denote the damping force in true and reconstruction model, respectively. In the damping error comparison, the error metric is displayed on the phase plane. As observed in Fig. 5 (a), the proposed method achieves higher damping force prediction accuracy compared to GMC-SINDy for $A_e = 5^\circ$. The proposed method maintains high accuracy, whereas GMC-SINDy exhibits significant prediction errors. As the excitation amplitude decreases to 1° and 0.5°, where the dynamic-to-static deformation response reduces to approximately 3% and 1%, GMC-SINDy fails to accurately predict the forces, showing acceptable error only near the two equilibria. This indicates that under LDSV phenomenon, GMC-SINDy can only capture localized features and is unable to predict global dynamics of the system. Conversely, the proposed method maintains accurate reconstruction of both forces even at these low amplitude ratios, demonstrating its robustness to the dynamic response amplitude.

Similarly, the robustness of the method to dynamic response amplitude is investigated for the position-dependent damping model. The reconstruction results under varying excitation amplitudes A_e are presented in Fig. 6. It can be observed that the proposed method maintains stable reconstruction accuracy as the excitation amplitude decreases, whereas the accuracy and effective range of GMC-SINDy deteriorate and eventually diminish. From the results in Figs. 5 and Fig. 6, it is concluded that, regardless of the damping

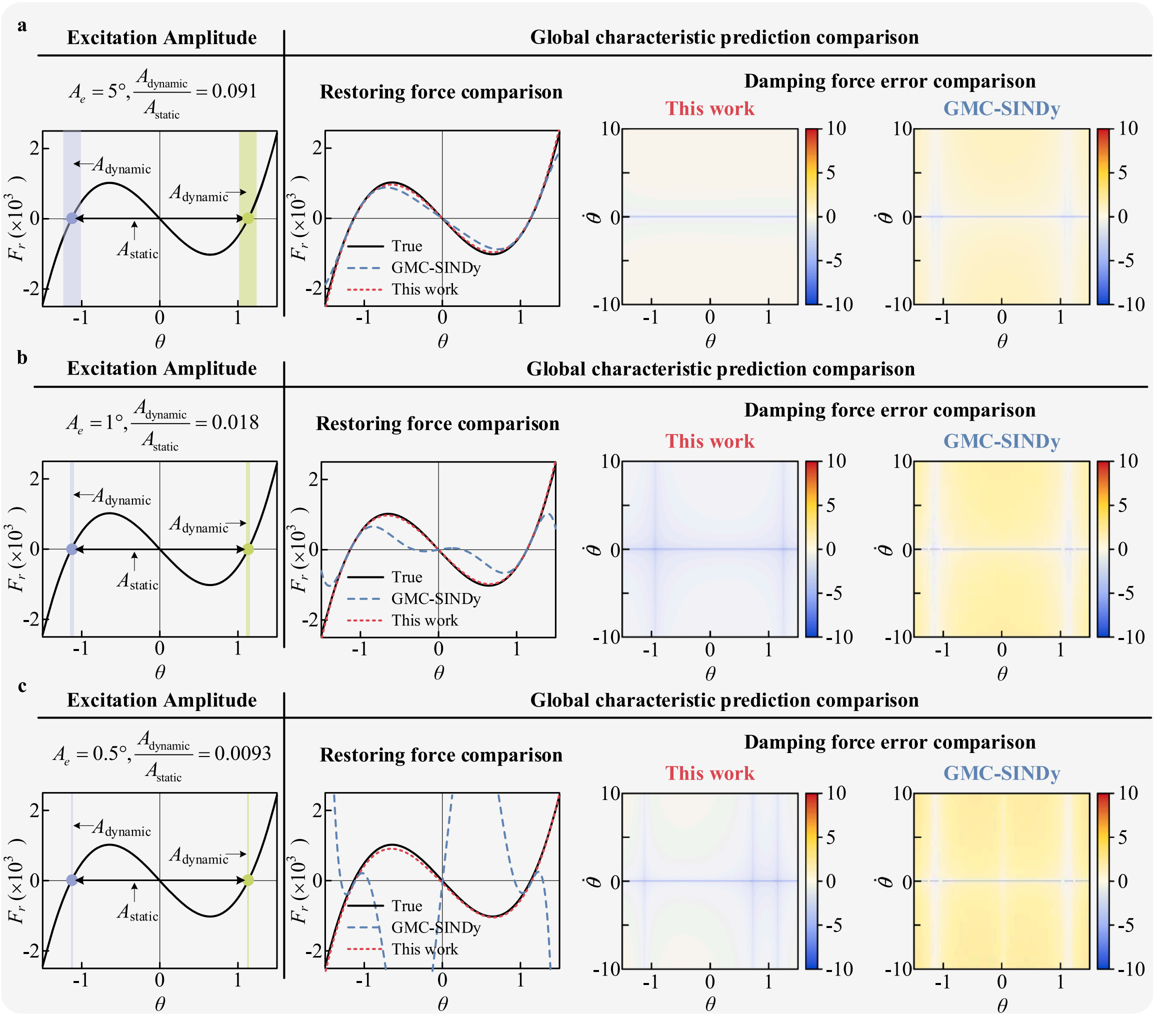

Fig. 6. Global model reconstruction results for position-dependent damping model under different excitation amplitudes A_e: (a) $A_e = 5^\circ$. (b) $A_e = 1^\circ$. (c) $A_e = 0.5^\circ$.

model, the proposed method is capable of accurately identifying the global dynamic model across a wide range of dynamic response amplitudes. This robustness lays the foundation for the accurate reconstruction of high-dimensional multi-stable systems, addressing the challenge outlined in Section 2.1.

3. Multi-stable and higher DOF systems

The application of the proposed method is extended to multi-stable systems with more equilibria and higher DOFs for further verification. In the first case, the local dynamic response data are obtained by numerically solving the governing equations. In the second case, an Adams model of an M-DOF multi-stable structure is established, and the local dynamic response data are acquired through Adams simulations. For the first case, our method employs 3rd-order local libraries for both resotring forces and damping forces, reconstructing up to 11th order globally, while GMC-SINDy uses 7th-order global libraries. This case highlights the advantage of the proposed method that low-order candidate libraries are sufficient for local fidelity near each equilibrium, yet the assembled global model achieves high-order expressive power without suffering from the numerical degradation that plagues the global high-order candidate libraries of GMC-SINDy. For the second case, both our method and GMC-SINDy adopt 5th-order libraries. This setting allows us to demonstrate that the proposed method avoids strong collinearity arising from multiple equilibrium positions in the global library. In both examples, zero-mean Gaussian white noise with a Signal-to-Noise Ratio (SNR) of 60 dB is added to simulate measurement noise.

3.1. An S-DOF tri-stable NES

The first case is the global model reconstruction of an S-DOF tri-stable NES system, proposed in Ref. [53]. The schematic diagram is shown in Fig. 7(a). Its governing equation writes

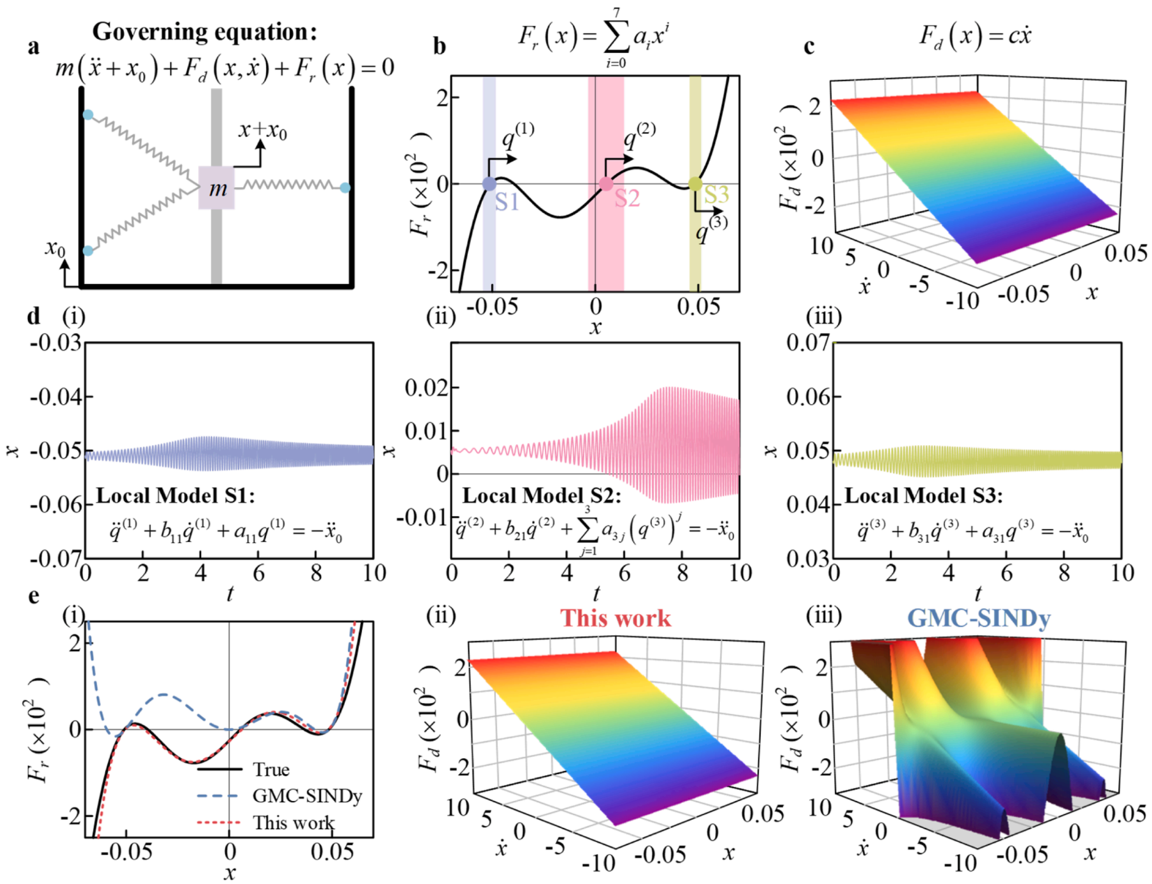

Fig. 7. Global model reconstruction of an S-DOF tri-stable NES. (a) Mechanical model and governing equation. (b) Restoring force-displacement relationship. (c) Expressions and damping force surfaces. (d) Intrawell dynamic response data collected near different equilibria and the expressions of the obtained lobal model. (f) Comparison of reconstructed models and global characteristic predictions.

$$m\left(\ddot{x}+\ddot{x}_0\right)+c\dot{x}+\sum_{i=0}^{7}\alpha_i x^i=0. \tag{23}$$

Following Ref. [53], the system parameters for the asymmetric tristable NES are selected accordingly and listed in Table 1 for completeness. The restoring force-displacement relationship and the damping force surface are shown in Figs. 7(b) and (c), respectively. As shown in Fig. 7(b), the restoring force of this NES features two key distinctions compared to the bistable bionic joint discussed in Section 2.3, which pose additional challenges for global model reconstruction. Firstly, it possesses three stable equilibria, one more than the previous case in terms of equilibria. Secondly, the restoring force is asymmetric, making it more complex than the symmetric bistable bionic joint. For the tri-stable NES shown in Fig. 7(a), base displacement excitations are applied near all three equilibria to acquire the intrawell dynamic responses data in Fig. 7(d). The amplitude ranges of the three sets of intrawell data are also indicated within the global restoring force curve in Fig. 7(b). Utilizing these data, local dynamic models near the three equilibria are constructed, with their mathematical expressions given in Fig. 7(d), and the reconstruction local model coefficients are listed in Table B3, Appendix B. Then, employing the global dynamic model construction described in Section 2.2.2, the global dynamic model of the tri-stable NES is obtained. For comparison, the GMC-SINDy method is also applied to the same data in Fig. 7(d) to reconstruct a global model. The reconstruction global model coefficients for both methods are listed in Table B4 in Appendix B. The restoring force F_r and damping force F_d reconstruction results obtained by the proposed method and GMC-SINDy are compared in Fig. 7(e).

It can be observed from Fig. 7(e) that the model reconstructed by GMC-SINDy exhibits significant errors in the region between the equilibria S1 and S2. This is attributed to the greater interwell separation between S1 and S2, combined with the smaller amplitude of the local response near S1. The more pronounced LDSV phenomenon in this region leads to increased errors in the GMC-SINDy reconstruction. In contrast, the proposed method achieves high accuracy in restoring force reconstruction, both within the intrawell and across the interwell ranges of all three equilibria. For the damping force, the proposed method accurately reconstructs the damping force surface, matching the true profile in Fig. 7(c) with high fidelity. Conversely, the damping force surface obtained by GMC-SINDy exhibits qualitative discrepancies from the ground truth. These results demonstrate the effectiveness of the proposed method for multi-stable systems with more equilibria and asymmetric constitutive relationships.

3.2. A 5-DOF multi-stable deployable structure

The second example is the global model reconstruction of a 5-DOF multi-stable deployable structure, as shown in Fig. 8(a). This structure is composed of multiple bistable tensegrity units connected in a serial configuration. Inspired by the Kresling origami pattern, the tensegrity unit is developed by replacing the creases in the Kresling origami structure with elastic trusses. Owing to identical geometric features with the Kresling origami, the definitions of its geometric parameters follow those in [54]. For each tensegrity unit, the geometric parameters and damping coefficients selected (as shown in Fig. 8(b)) yield the schematic diagrams of the restoring force constitutive relationship and damping force surface, presented in Figs. 8(c) and (d), respectively. Subjected to a base displacement excitation at the fully folded and fully deployed configurations, schematic diagrams of the dynamic response for each unit are shown in Fig. 8(e). The amplitudes of the dynamic response near these two configurations for each unit are denoted as A_{1i} and A_{2i}, respectively. The amplitude ratios of dynamic response to the static deformation between two equilibria for each unit are also listed in Fig. 8(b). As revealed in Fig. 8(b), the amplitude ratio gradually decreases as the base excitation propagates upward from the bottom. This demonstrates that obtaining large-amplitude dynamic responses is challenging for such a high-dimensional multi-stable system, highlighting the importance of achieving global model reconstruction from local dynamic information.

The intrawell dynamic response data from Fig. 8(e) are utilized as training data for both the proposed method and GMC-SINDy. The global model reconstruction results from both methods are shown in Fig. 9. All coefficients of reconstruction local and global models are presented in Tables B5 and B6 in Appendix B. In the reconstruction of the restoring terms, GMC-SINDy only identifies the equilibrium positions of each unit, losing important intrawell and interwell dynamic features such as the stiffness near equilibria, energy barrier, and stability of the equilibria. In contrast, the proposed global model reconstruction method demonstrates high accuracy for predicting restoring force across the entire deformation range. For the reconstruction of the damping terms, the error of the proposed method is maintained at a low level throughout the entire phase plane, demonstrating its effectiveness in reconstructing the damping force for each unit. As an indicative quantification, the error of the GMC-SINDy is several orders of magnitude higher than that of the proposed method. This reconfirms the previous conclusion: the strong collinearity of the restoring force terms in the library function matrix not only leads to the failure of restoring force reconstruction but also simultaneously causes the failure of damping force reconstruction. These results not only demonstrate the feasibility of the proposed method for high-dimensional multi-stable systems but also reveal its robustness against the amplitude variation of the dynamic response in the training data.

To demonstrate the capability of the proposed method in predicting the dynamic behavior of M-DOF multi-stable structures, the obtained global model is applied to predict both intrawell and interwell dynamic behavior of the 5-DOF multi-stable deployable structure. First, the displacement transmissibility T_d of the multi-stable deployable structure under specific configurations is analyzed,

Table 1
System parameters of the asymmetric tri-stable NES adopted from Ref. [53].

m (kg)	c (N•s•m^{-1})	α_0 (N)	α_1 (N•m^{-1})	α_2 (N•m^{-2})	α_3 (N•m^{-3})	α_4 (N•m^{-4})	α_5 (N•m^{-5})	α_6 (N•m^{-6})	α_7 (N•m^{-7})
3.5×10^{-2}	0.8	-0.9	168.6	575.1	-2.0×10^{5}	-5.0×10^{4}	6.5×10^{7}	7.6×10^{5}	-4.7×10^{9}

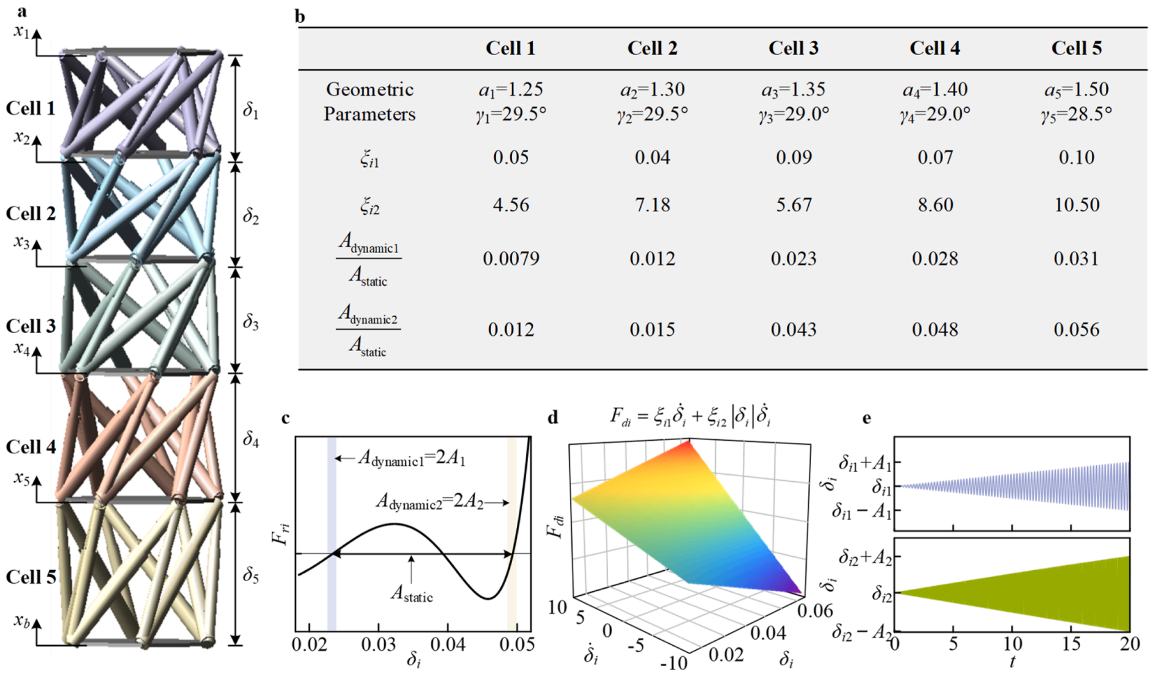

	Cell 1	Cell 2	Cell 3	Cell 4	Cell 5
Geometric Parameters	a_1=1.25 γ_1=29.5°	a_2=1.30 γ_2=29.5°	a_3=1.35 γ_3=29.0°	a_4=1.40 γ_4=29.0°	a_5=1.50 γ_5=28.5°
ξ_{i1}	0.05	0.04	0.09	0.07	0.10
ξ_{i2}	4.56	7.18	5.67	8.60	10.50
$\frac{A_{\text{dynamic1}}}{A_{\text{static}}}$	0.0079	0.012	0.023	0.028	0.031
$\frac{A_{\text{dynamic2}}}{A_{\text{static}}}$	0.012	0.015	0.043	0.048	0.056

Fig. 8. Schematic diagram and data acquisition process of a 5-DOF multi-stable deployable structure. (a) The Adams simulation model and the corresponding global coordinate system definition. (b) Structural parameters, damping parameters, and ratio of dynamic response amplitude to static deformation for the 5-DOF system. The representative schematic diagram of (c) Restoring force-displacement relationship, (d) Damping force surface, and (e) Collected intrawell dynamic response data.

which is defined as

$$T_d = 20\log_{10}\left(\frac{x_1}{x_b}\right), \tag{24}$$

where x_1 and x_b are the displacement of distal end and base as defined in Fig. 8(a). Here, the displacement transmissibility under the fully folded and the fully deployed configurations is considered. Sinusoidal base displacement excitations with an amplitude of 1 mm at different frequencies f_e are applied in both reconstructed global model and Adams simulation model, within the frequency range of 0.5-10 Hz. The comparisons of displacement transmissibility obtained by the reconstructed global model and Adams simulation model under the fully folded and fully deployed configurations are shown in Fig. 10(a) and (c), and the corresponding time-domain responses at f_e=0.5 Hz, 1.5 Hz, and 2.5 Hz are also compared in Fig. 10(b) and (d). Under both configurations, high consistency is observed between the predictions of the global reconstructed model and the Adams simulation model for both the natural frequencies and the displacement transmissibility at different frequencies. This demonstrates that the proposed global model reconstruction method effectively preserves the intrawell restoring and damping force characteristics from the local models.

Furthermore, to validate the capability of the global model reconstruction method for predicting the global dynamic behavior of high-dimensional multi-stable systems, the deployment of the multi-stable deployable structure is considered. The deployment process of deployable structures is a transient global dynamic process involving energy transfer between different cells and energy barriers crossing. Accurate prediction of the deployment process relies not only on the accurate capture of intrawell features by the global model but also on the precise construction of the global restoring and damping force characteristics, which further demonstrates the effectiveness of the global dynamic model construction. As shown in Fig. 11(a), the base of the multi-stable deployable structure is fixed, while the top is subjected to a time-varying force actuation to switch from the fully folded configuration to different deployed configurations. The actuation force is assumed to satisfy the following expression:

$$F(t) = \begin{cases} A\sin(2\pi f t), t \leq \dfrac{1}{2f} \\ 0, t >\leq \dfrac{1}{2f} \end{cases}, \tag{25}$$

where A is the amplitude of the force actuation; and f the actuation frequency, which determines the time duration of the actuation. When f is low (e.g., $f = 0.05$ Hz), the duration of the force actuation is long, and the deployment process approximates a quasi-static process. On the contrary, a higher (e.g., $f = 4.5$ Hz) mimics an impact-like load, making the deployment a dynamic transient process.

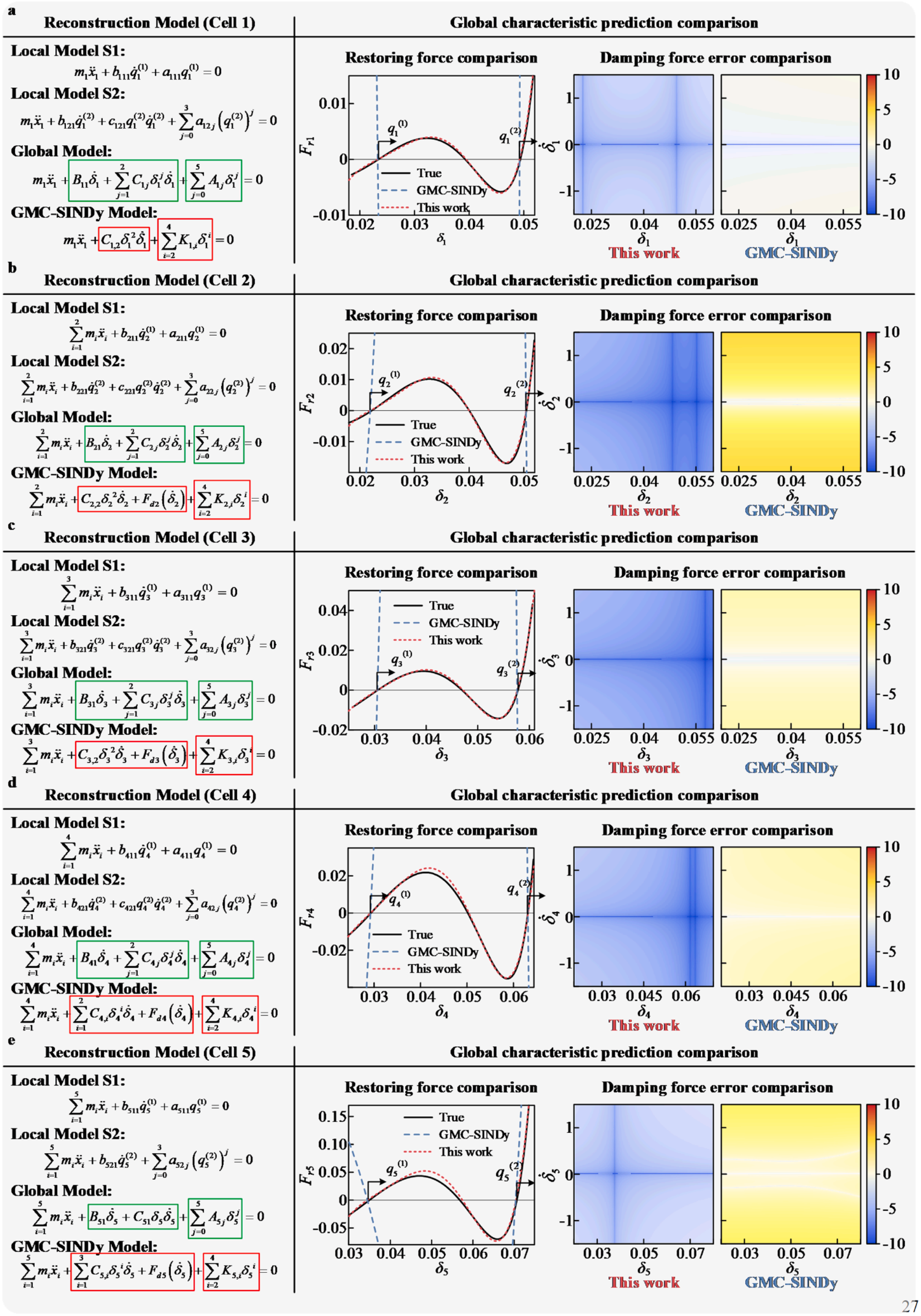

Fig. 9. Reconstruction model and global characteristic prediction comparison of a 5-DOF multi-stable deployable structure. (a) Cell 1. (b) Cell 2. (c) Cell 3. (d) Cell 4. (e) Cell 5.

Utilizing the reconstructed global model, the deployment processes under different amplitudes A and frequencies f are analyzed. The basins of attraction corresponding to different deployed configurations are shown in Fig. 11(a). Each configuration represented by a specific color is detailed in Fig. 11(b). According to the results in Fig. 11(a), under quasi-static actuation ($f < 0.5$ Hz) and impact actuation ($f > 4.5$ Hz), each unit of the 5-DOF multi-stable deployable structure is sequentially deployed according to stiffness from low to high, enabling a total of five distinct deployed configurations. When the frequency f lies between the quasi-static and impact actuation regimes, more complex deployed configurations can be achieved. To demonstrate the accuracy of the obtained basins of attraction, Adams simulations are performed for the deployment processes under 15 sets of actuation parameters (f, A), with results

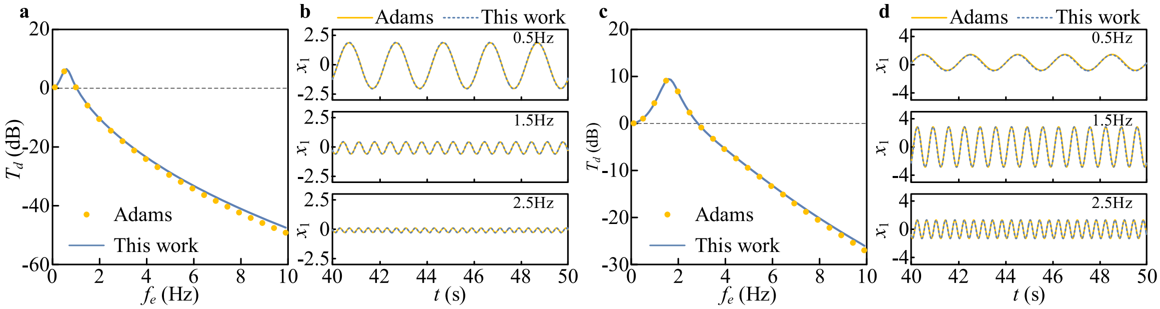

Fig. 10. Prediction of intrawell vibration displacement transmissibility under different configurations (a, b) Frequency response and time-history response under fully folded configuration. (c, d) Frequency response and time-history response under fully deployed configuration.

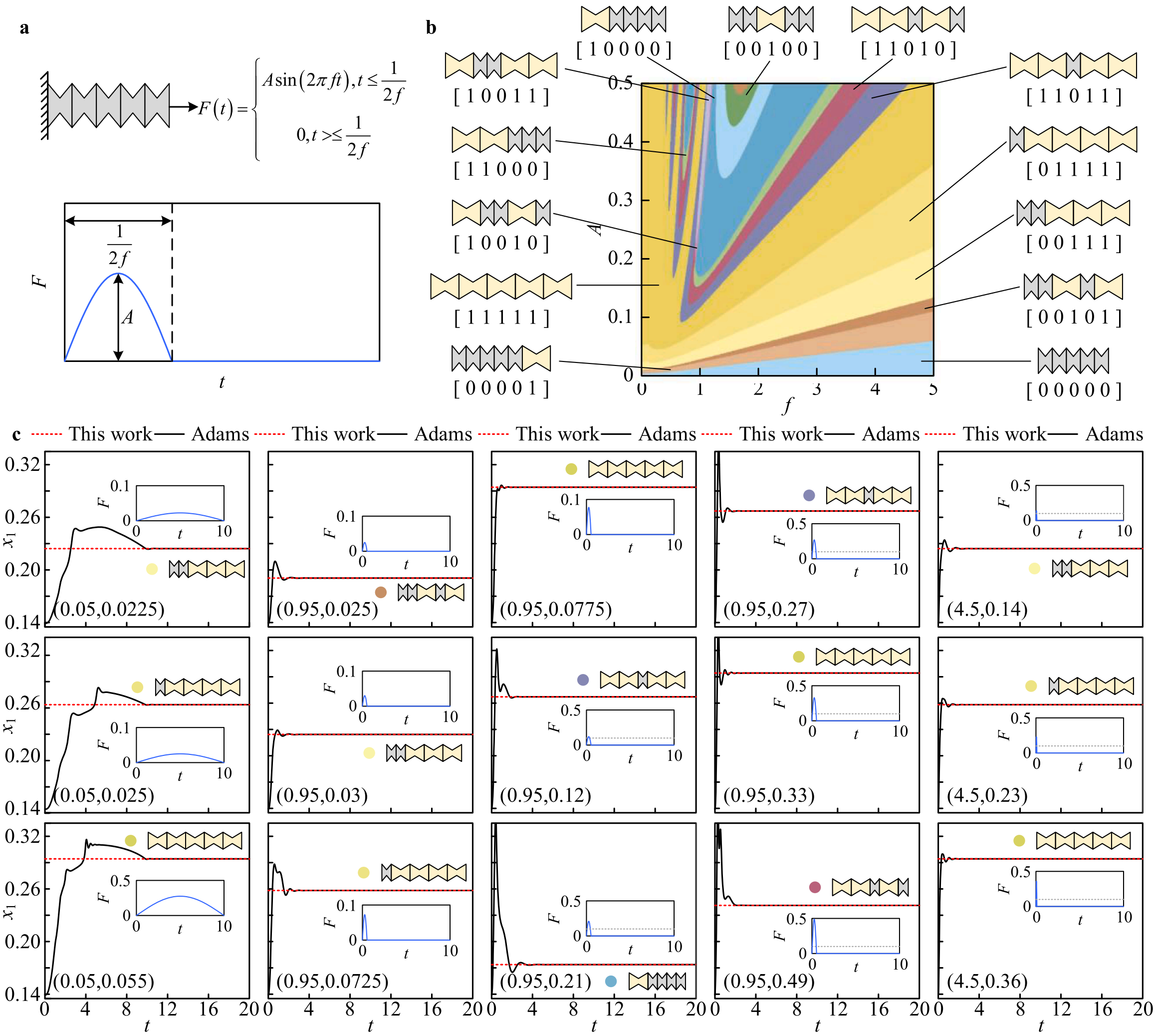

Fig. 11. Deployment conditions prediction for multi-stable deployable structures under force actuation. (a) Schematic diagram of the deployment actuation process. (b) Basins of attraction corresponding to different deployed configurations. (c) Comparison between predicted deployment configuration and actual deployment process under different actuation parameters.

shown in Fig. 11(d). In this figure, the red dashed lines represent the predicted end positions from the reconstructed global model, while the black solid lines denote the transient deployment time-history curves obtained from Adams simulations. Additionally, the time-history curve of the actuation force F for each parameter set is also shown. The first and fifth column correspond to the quasi-static and impact actuation cases, respectively, while the second to fourth columns correspond to the intermediate cases between these two regimes. It can be observed that under different force actuation conditions, the predictions of the reconstructed global model agree with the Adams simulation results. This consistency demonstrates the potential application of the proposed global model reconstruction method to design and optimize the actuation of high-dimensional multi-stable systems.

4. Experimental verifications

In this section, the proposed method is applied to an M-DOF multi-stable deployable structure, shown in Fig. 12(a), for experimental verifications. The structure is composed of multiple bistable truss units inspired by Kresling origami, fabricated using Polyjet 3D printing technology [55]. The rigid white rods are made of VeroPureWhite with Young's modulus of 65 MPa, and the black flexible joints are made of Agilus with Shore hardness of 40 and 50. As shown in Fig. 12(b), each truss unit has two stable configurations: fully folded and fully deployed. Lateral bending is prevented by installing a smooth guiding rod along the central axis of the structure, with linear bearings mounted at the center of each acrylic connecting plate. This configuration constrains lateral motion while allowing free axial sliding, ensuring that the motion of the structure is confined to the axial direction. To collect dynamic response data near these equilibria, the testing setup illustrated in Fig. 12(c) is constructed. A low-frequency shaker provides base displacement excitation. The excitation signal is generated by a signal generator, amplified, and then fed to the shaker. Accelerometers measure the base excitation and the responses at the end of each unit, with data recorded by a data acquisition system. For the fully folded configuration, dynamic responses are collected under sinusoidal base excitations at 4, 5, and 6 Hz. For the fully deployed configuration, excitations at 8, 9, and 10 Hz are used. The acceleration signals are numerically integrated to obtain the deformation of each unit, as shown in Fig. 12(d). It can be observed that the dynamic response amplitudes are much smaller than the interwell deformation from the folded to the deployed states. This highlights the challenge in acquiring large-amplitude global responses and underscores the necessity of the proposed method, which uses only small-amplitude data.

Using the collected data, the dynamic model is reconstructed via the proposed method and GMC-SINDy. For the experimental validation, our method employs 3rd-order local candidate libraries, while GMC-SINDy uses 7th-order global candidate libraries. The results shown in Fig. 13, and corresponding coefficients are illustrated in Tables B7 and B8, Appendix B. It follows that the proposed

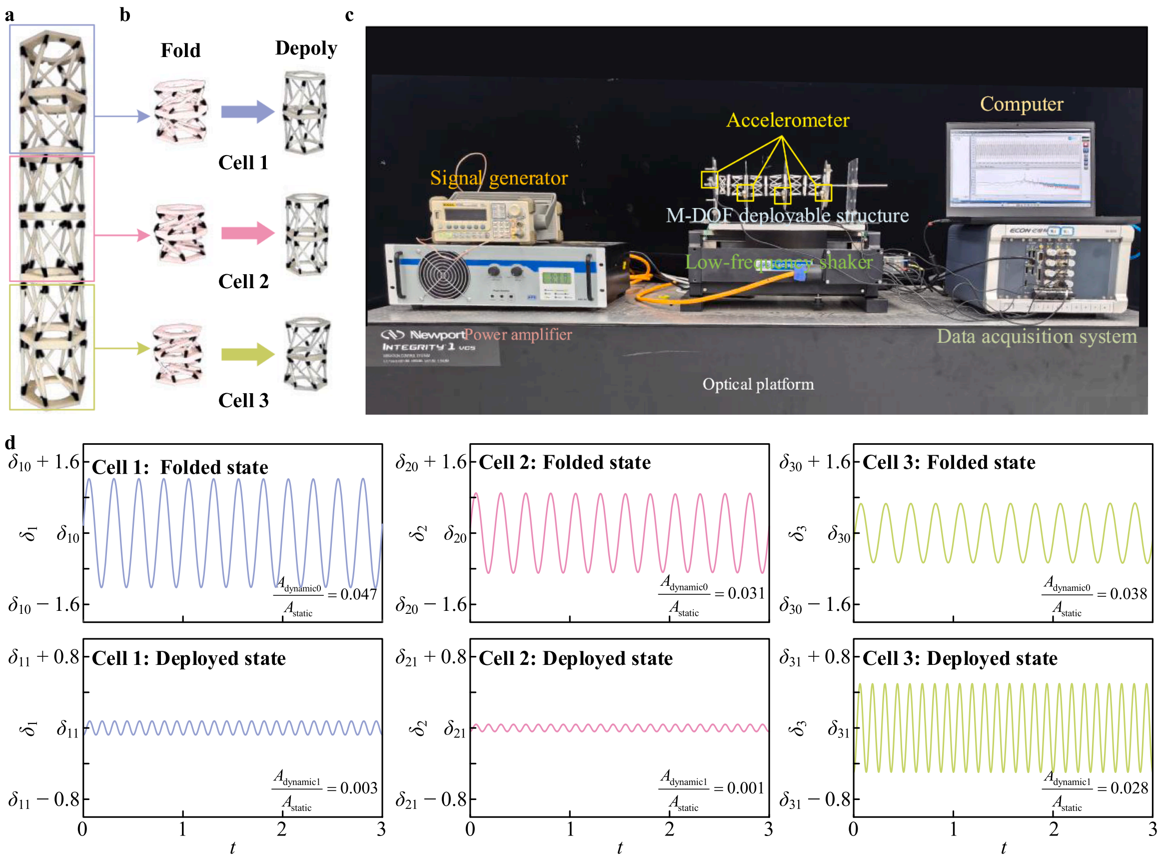

Fig. 12. Experimental setup and dynamic response data for the M-DOF multi-stable deployable structure. (a) Experimental prototype. (b) Bistable truss unit in folded and deployed states. (c) Schematic of the dynamic test setup. (d) Acquired intrawell dynamic response data near the folded and deployed equilibria.

method successfully identifies the restoring and damping force models for all units. In contrast, GMC-SINDy fails to identify the damping force of Cell 1 and the restoring force of Cell 3. The prediction errors of both methods on the training data are quantified in Table 2 using the R^2 and Normalized Root Mean Square Error (NRMSE) metrics. The proposed method achieves high prediction accuracy, significantly outperforming GMC-SINDy.

Furthermore, the predictive capability of the global model for both local and global dynamics is validated. First, the acceleration transmissibility under configurations 0-0-1 and 1-1-0 is predicted, where 0 and 1 denote the folded and deployed states of a unit, respectively. The acceleration transmissibility and time-domain responses at selected frequencies are compared in Fig. 14(a-b) for configuration 0-0-1 and in Fig. 14 (e-f) for configuration 1-1-0. For both configurations, the global model predictions show high consistency with experimental results across frequencies, whereas the GMC-SINDy model entails large errors. Notably, for the 1-1-0 configuration, the GMC-SINDy prediction diverges in the 2.9–3.75 Hz range. This divergence stems from unphysical negative damping identified in the GMC-SINDy model. This demonstrates the global model's ability to capture local dynamics, even for configurations outside the training data, verifying the effectiveness of the proposed method. Additionally, for the 0-0-1 and 1-1-0 configurations, Fig. 14(c) and (g) show the peaks of the power spectral density (PSD) for the three modes at different excitation frequencies, respectively. The PSD peaks predicted by the global model show high consistency with experimental measurements. The variations in PSD peaks ratios and mode shapes between configurations reflect the inherent nonlinearity of the structure. These results demonstrate the method's capability to predict the overall structural dynamics.

Finally, we verify the global dynamic prediction capability of the method by predicting the deployment process using the

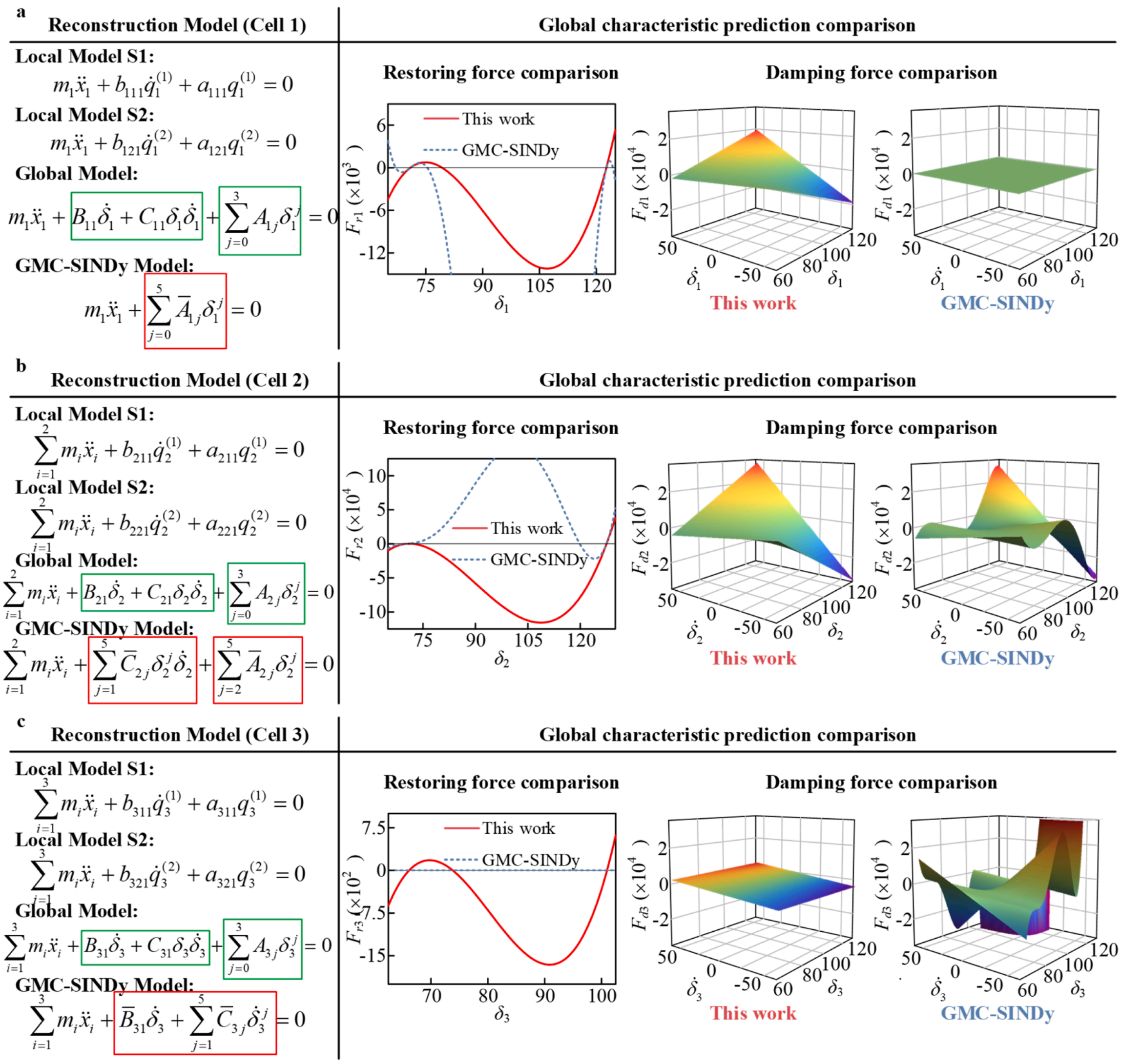

Fig. 13. Comparison of reconstructed models for the experimental prototype. (a) Cell 1. (b) Cell 2. (c) Cell 3. Each panel shows the identified local model equations, global model equation, and a comparison of the restoring force (2D plot) and damping force (3D surface) against the true characteristics.

Table 2
Prediction errors of global model and GMC-SINDy on the training data under different configurations.

Training data configuration	Cell No.	Global model		GMC-SINDy model	
		R^2	NRMSE	R^2	NRMSE
0-0-0	1	0.9992	0.082%	0.2590	74.10%
	2	0.9974	0.26%	0.9974	0.26%
	3	0.9989	0.11%	0.9944	0.56%
1-1-1	1	0.9989	0.11%	0.0116	98.84%
	2	0.9980	0.20%	0.9980	0.20%
	3	0.9920	0.80%	0.9728	0.27%

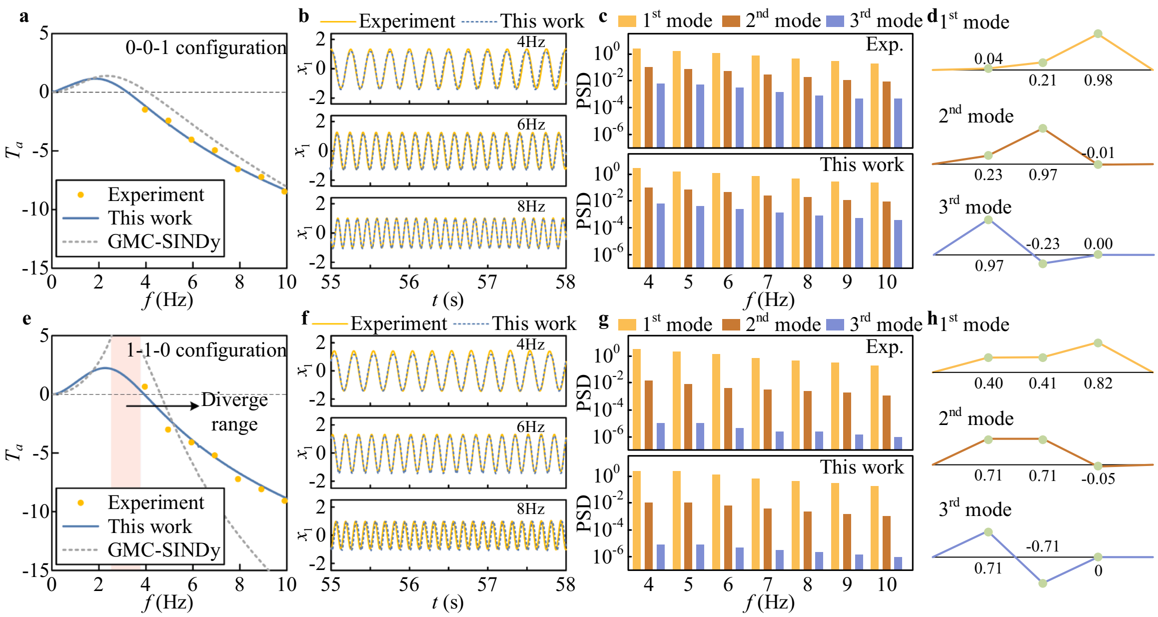

Fig. 14. Prediction of acceleration transmissibility and modal characteristics. (a, b) Frequency response and time-history for configuration 0-0-1. (c) PSD peaks of three modes at different frequencies for configuration 0-0-1. (d) Mode shapes for configuration 0-0-1. (e, f) Frequency response and time-history for configuration 1-1-0. (g) PSD peaks of three modes for configuration 1-1-0. (h) Mode shapes for 1-1-0.

experimental setup shown in Fig. 15(a). The structure starts in the fully folded configuration 0-0-0. A manually applied actuation force is applied at its tip via a string to trigger deployment. A force sensor at the tip records the actuation force time-history. Figure 15(b) shows the two possible final configurations deployed and undeployed. The measured force is input into the global model to predict the deployment process, schematically compared in Fig. 15(c). The prediction is compared with the actual final configuration. Six deployment tests are conducted. The deployment process is detailly illustrated in Video S1 in the Supplementary material. Fig. 15(d) shows the actuation force and the corresponding deployment process for all six cases. The predicted deployment processes show excellent agreement with experiments, accurately capturing the dynamic deployment behavior. This validates the method's effectiveness in capturing global dynamics and its robust predictive performance for high-dimensional multi-stable systems.

5. Conclusions

This study proposes a method for reconstructing global models of dynamic systems with multiple stable states, specifically tackling the challenge of inferring global dynamics from local dynamic information using only small-amplitude responses. The method resolves the inherent conflict between large static deformations and small vibration amplitudes in multi-stable systems by fusing local dynamic models through coordinate coordination. First, instead of reconstructing the dynamic model within a single global coordinate frame, we construct multiple local dynamic models around distinct stable equilibria. This avoids the strong collinearity introduced by large static deformations, which is inherent to representations in a global coordinate system. Second, by exploiting the principle of coordinate coordination, these local models are used to recover the higher-order nonlinear terms of the global model. Such terms are typically missing from local models because of their minor influence on small-amplitude responses. Numerical examples verify the method's effectiveness for high-dimensional nonlinear systems with multiple equilibria, demonstrating its robustness to the amplitude of the training dynamic data. Experimental validation was performed on an M-DOF multi-stable deployable structure inspired by the Kresling origami pattern. The proposed method successfully identified both the restoring and damping forces for all units, achieving

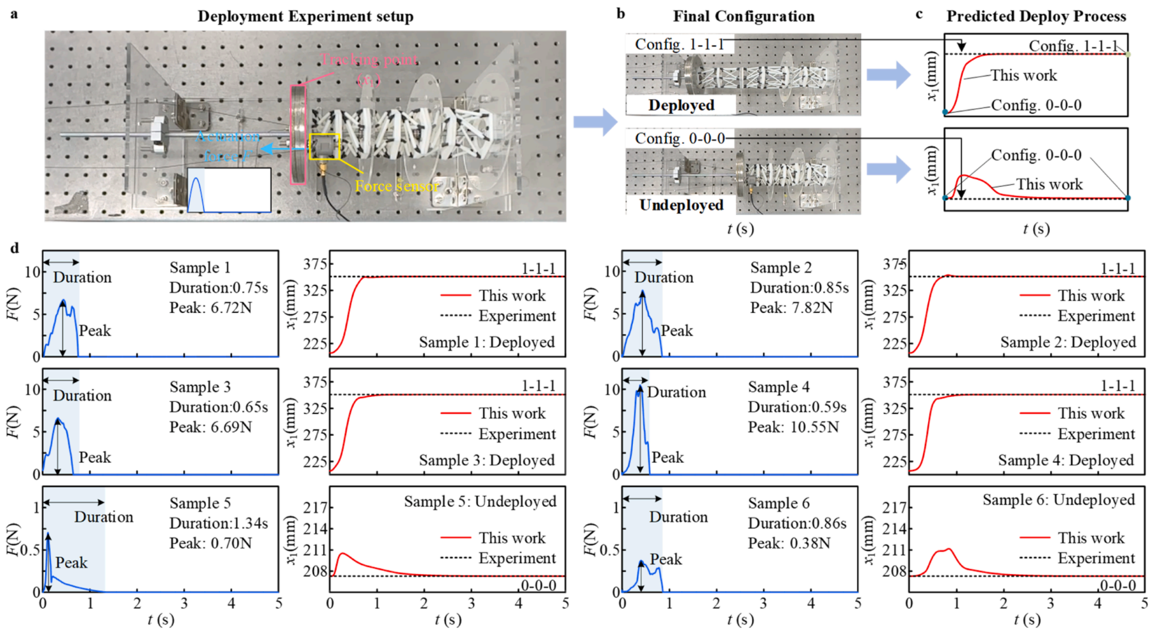

Fig. 15. Deployment process prediction and validation. (a) Experiment setup for deployment. (b) Final deployed and undeployed configurations. (c) Schematic of the comparison methodology. (d) Comparison of predicted model and actual experiment deployment processes under six different actuation conditions.

high predictive accuracy on the training data (NRMSE $<$ 1%, $R^2 > 0.99$). In contrast, the benchmark GMC-SINDy method failed to capture the damping force of Cell 1 and the restoring force of Cell 3. The global model's effectiveness in predicting both local and global dynamics is further demonstrated through predictions of acceleration transmissibility and deployment states. For configurations absent from the training data, the model successfully predicted the structure's acceleration transmissibility, surmising the generalizable feature of the captured local dynamic characteristics. Furthermore, the global model accurately predicted the peak PSD values corresponding to the three modes under different configurations, underscoring the method's effectiveness in predicting the overall structural dynamics of multi-stable systems. Successful deployment predictions under six distinct actuation conditions further confirm the model's capacity to capture global dynamic behaviors. This method provides a practical framework for model reconstruction of high-dimensional multi-stable systems, with potential applications in deployable structures, robotics, and mechanical computing.

CRediT authorship contribution statement

Jiawei Qian: Writing – original draft, Visualization, Software, Methodology, Investigation, Formal analysis, Data curation, Conceptualization. **Li Cheng:** Writing – review & editing, Validation, Supervision, Project administration, Funding acquisition, Conceptualization. **Xiuting Sun:** Writing – review & editing, Visualization, Validation, Supervision, Project administration, Funding acquisition, Conceptualization. **Qian Lv:** Software, Investigation. **Jian Xu:** Supervision, Resources, Project administration, Funding acquisition.

Declaration of competing interest

The authors declare that they have no known competing financial interests or personal relationships that could have appeared to influence the work reported in this paper.

Acknowledgements

The authors would like to acknowledge the support from the National Natural Science Foundation of China under Grants (No. U2441202, 12372043, 12372022) and Fundamental Research Funds for Central Universities. The work also benefited from the support of the RIAIoT (Research Institute for Artificial Intelligence of Things) through project P0049625.

Supplementary materials

Supplementary material associated with this article can be found, in the online version, at doi:10.1016/j.jsv.2026.120053.

Appendix A. Collinearity of polynomial coefficient terms

Under periodic excitation, the dynamic response of a multi-stable system can be represented by Fourier series

$$x(t) = A_0 + \sum_{i=1}^{k} A_i \sin(\omega_i t + \varphi_i), \tag{A.1}$$

where A_0 and A_i are the Fourier coefficients. A_0 represents the static equilibrium position; and A_i the vibration amplitude at different frequencies. If LDSV phenomenon exists, the static equilibrium position is significantly larger than the vibration amplitude, and thus vibration amplitude can be expressed as

$$A_i = \varepsilon \overline{A}_i, i = 1, 2, ..., k, \tag{A.2}$$

where ε denotes a small quantity, and $\overline{A}_i$ is of the same order as the static equilibrium position A_0. Thus, the higher-order displacement terms can be written as

$$x^n(t) = \sum_{m=1}^{n} C_n^m A_0^{n-m} \left(\sum_{i=1}^{k} \varepsilon \overline{A}_i \sin(\omega_i t + \varphi_i) \right)^m = A_0^n + n\varepsilon A_0^{n-1} \left(\sum_{i=1}^{k} \overline{A}_i \sin(\omega_i t + \varphi_i) \right) + o(\varepsilon). \tag{A.3}$$

Since the static component A_0^n in x^n is much larger than the dynamic component, x^n under discrete-time sampling can be regarded as a constant vector $\mathbf{c}_n$. Thus, the correlation coefficient between any two terms in the polynomial representation of the restoring force is

$$\rho_{p,q} = \frac{\langle \mathbf{x}^p, \mathbf{x}^q \rangle}{\| \mathbf{x}^p \| \cdot \| \mathbf{x}^q \|} \approx \frac{\langle \mathbf{c}_p, \mathbf{c}_q \rangle}{\| \mathbf{c}_p \| \cdot \| \mathbf{c}_q \|} \to 1. \tag{A.4}$$

This indicates that the two terms exhibit extremely strong collinearity, which will cause the condition number of the library function matrix to approach positive infinity

$$\kappa(\boldsymbol{\Theta}) = \frac{\lambda_{\max}}{\lambda_{\min}} \geq \frac{\lambda_{\max}}{1 - \rho_{p,q}} \to \infty. \tag{A.5}$$

Appendix B. Identified model coefficients for all cases

Table B1
Reconstruction local model coefficients for the baseline bistable bionic joint.

Terms	Position-independent damping		Position-dependent damping	
	Local model S1	Local model S2	Local model S1	Local model S2
$q^{(i)}$	4.487×10^3	4.487×10^3	4.489×10^3	4.490×10^3
$(\dot{q}^{(i)})^3$	10.001	9.998	N/A	N/A
$\dot{q}^{(i)}$	N/A	N/A	63.944	63.945
$q^{(i)}\dot{q}^{(i)}$	N/A	N/A	113.100	113.095

Table B2
Reconstruction global model coefficients for the baseline bistable bionic join.

Terms	Position-independent damping		Position-dependent damping	
	This work	GMC-SINDy	This work	GMC-SINDy
1	-0.085	N/A	0.249	N/A
θ	-2.244×10^3	-9.449×10^4	-2.245×10^3	0.388×10^3
θ^2	0.007	N/A	-0.230	N/A
θ^3	1.755×10^3	2.183×10^5	1.755×10^3	-4.542×10^3
θ^5	N/A	-1.693×10^5	N/A	5.015×10^3
θ^7	N/A	4.408×10^4	N/A	-1.330×10^3
$(\dot{\theta}^{(i)})^3$	9.999	N/A	N/A	N/A
$\dot{\theta}^{(i)}$	N/A	-1.781×10^4	-0.005	0.584×10^3
$\theta\dot{\theta}^{(i)}$	N/A	N/A	-0.003	N/A
$\theta^2\dot{\theta}^{(i)}$	N/A	2.792×10^4	50.004	-1.312×10^3
$\theta^3\dot{\theta}^{(i)}$	N/A	N/A	9.847×10^{-4}	N/A

(continued on next page)

Table B2 (*continued*)

Terms	Position-independent damping		Position-dependent damping	
	This work	GMC-SINDy	This work	GMC-SINDy
$\theta^4\dot{\theta}^{(i)}$	N/A	-1.092 $\times$ 10^4	N/A	1.059 $\times$ 10^3
$\theta^6\dot{\theta}^{(i)}$	N/A	N/A	N/A	-0.274 $\times$ 10^3

Table B3
Reconstruction local model coefficients for the S-DOF tri-stable NES.

Terms	Local model S1	Local model S2	Local model S3
$q^{(i)}$	0.927	1.046	0.911
$(q^{(i)})^2$	N/A	-0.124	N/A
$(q^{(i)})^3$	N/A	-0.122	N/A
$\dot{q}^{(i)}$	0.335	0.3348	0.383

Table B4
Reconstruction global model coefficients for the S-DOF tri-stable NES.

Terms	This work	GMC-SINDy
1	-26.882	N/A
x	4.432 $\times$ 10^3	N/A
x^2	2.959 $\times$ 10^4	2.592 $\times$ 10^5
x^3	-4.355 $\times$ 10^6	-1.276 $\times$ 10^6
x^4	-1.362 $\times$ 10^7	-1.283 $\times$ 10^8
x^5	9.433 $\times$ 10^8	5.197 $\times$ 10^8
x^6	2.880 $\times$ 10^9	2.624 $\times$ 10^{10}
x^7	4.065 $\times$ 10^{10}	N/A
$\dot{x}$	22.848	N/A
$x\dot{x}$	0.082	N/A
$x^2\dot{x}$	3.466	1.642 $\times$ 10^5
$x^4\dot{x}$	N/A	-1.246 $\times$ 10^8
$x^5\dot{x}$	N/A	2.799 $\times$ 10^6
$x^6\dot{x}$	N/A	2.496 $\times$ 10^{10}

Table B5
Reconstruction local model coefficients for the 5-DOF multi-stable deployable structure.

Terms	Local model S1					Local model S2				
	1	2	3	4	5	1	2	3	4	5
1×10^{-3}	N/A	N/A	N/A	N/A	N/A	-0.013	-0.064	-0.367	-1.209	-3.704
$q^{(i)}$	0.504	0.811	1.565	2.394	5.016	0.393	0.878	0.847	1.692	3.462
$(q^{(i)})^2 \times 10^3$	N/A	N/A	N/A	N/A	N/A	0.803	1.442	1.599	2.659	5.377
$(q^{(i)})^3 \times 10^5$	N/A	N/A	N/A	N/A	N/A	0.549	0.793	0.998	1.382	2.762
$\dot{q}^{(i)}$	0.157	0.197	0.263	0.326	0.465	0.275	0.438	0.417	0.617	0.841
$q^{(i)}\dot{q}^{(i)} \times 10^1$	N/A	N/A	N/A	N/A	N/A	0.005	0.007	0.057	0.086	N/A

Table B6
Reconstruction global model coefficients for the 5-DOF multi-stable deployable structure.

Terms	This work					GMC-SINDy				
	1	2	3	4	5	1	2	3	4	5
1×10^1	-0.342	-0.346	-1.487	-1.515	-7.546	N/A	N/A	N/A	N/A	N/A
$\delta_i \times 10^2$	0.602	0.609	2.094	2.128	8.808	N/A	N/A	N/A	N/A	N/A
${\delta_i}^2 \times 10^4$	-0.426	-0.429	-1.189	-1.204	-4.110	0.692	-0.185	-0.667	-0.313	0.156
${\delta_i}^3 \times 10^5$	1.487	1.483	3.361	3.372	9.498	-4.381	1.191	3.341	1.569	-0.674
${\delta_i}^4 \times 10^7$	-0.254	-0.246	-0.467	-0.459	-1.077	0.604	-0.155	-0.379	-0.170	0.064
${\delta_i}^5 \times 10^7$	1.673	1.558	2.528	2.413	4.764	N/A	N/A	N/A	N/A	N/A
$\mathrm{sign}(\dot{\delta}_i)$	N/A	N/A	N/A	N/A	N/A	N/A	0.019	0.041	0.005	0.010
$\dot{\delta}_i^2(10^2)$	N/A	N/A	N/A	N/A	N/A	N/A	7.951	0.284	-0.068	0.930
$\dot{\delta}_i^3\ (10^4)$	N/A	N/A	N/A	N/A	N/A	N/A	-1.773	N/A	N/A	-0.069
$\dot{\delta}_i \times 10^{-2}$	5.273	4.147	8.996	7.422	10.419	N/A	N/A	N/A	N/A	N/A
$\delta_i\dot{\delta}_i \times 10^0$	4.441	7.180	5.670	8.606	10.481	N/A	N/A	N/A	$>10^2$	$>10^3$
$\delta_i^2\dot{\delta}_i \times 10^0$	1.612	0.014	-0.009	-0.046	N/A	11.415	$>10^3$	$>10^3$	$>10^3$	$>10^5$
$\delta_i^3\dot{\delta}_i \times 10^{-3}$	N/A	N/A	N/A	N/A	N/A	N/A	N/A	N/A	N/A	$>10^9$

Table B7
Reconstruction local model coefficients for experimental verification.

Terms	Local model S1			Local model S2		
	1	2	3	1	2	3
$q^{(i)}$	394.211	480.852	103.947	2.038×10^3	1.386×10^4	0.368×10^3
$\dot{q}^{(i)}$	22.229	32.814	51.528	339.489	634.087	62.740

Table B8
Reconstruction global model coefficients for experimental verification.

Terms	This work			GMC-SINDy		
	1	2	3	1	2	3
1×10^6	-0.627	-2.819	-0.192	47.512	-49.672	N/A
$\delta_i \times 10^5$	0.218	1.014	0.074	-277.795	29.286	N/A
$\delta_i^2 \times 10^3$	-0.248	-1.178	-0.094	63.912	-67.970	N/A
δ_i^3	0.909	4.368	0.390	-721.989	774.440	N/A
δ_i^4	N/A	N/A	N/A	3.999	-4.324	N/A
$\delta_i^5 \times 10^{-3}$	N/A	N/A	N/A	-8.686	9.455	N/A
$\dot{\delta}_i$	-412.711	-703.771	30.223	N/A	N/A	1.332×10^6
$\delta_i\dot{\delta}_i$	6.133	10.493	0.322	N/A	-463.8863	-8.599×10^4
$\delta_i^2\dot{\delta}_i$	N/A	N/A	N/A	N/A	20.956	2.201×10^3
$\delta_i^3\dot{\delta}_i$	N/A	N/A	N/A	N/A	-0.346	-27.890
$\delta_i^4\dot{\delta}_i$	N/A	N/A	N/A	N/A	0.175	0.002
$\delta_i^5\dot{\delta}_i \times 10^{-4}$	N/A	N/A	N/A	N/A	-4.339	-0.064

Data availability

Data will be made available on request.

References

[1] S. Gao, F. Jiang, X. Sun, P. Qi, J. Xu, Curved bistable origami-inspired flexible transcatheter mitral valve clamping, Adv. Sci. 13 (2026) e17350, https://doi.org/10.1002/advs.202517350.
[2] Z. Qi, X. Sun, J. Xu, A kirigami multi-stable flexible gripper with energy-free configurations switching, Adv. Intell. Syst. 6 (2024) 2400038, https://doi.org/10.1002/aisy.202400038.
[3] D. Michalaros, C.C. Addis, J. Rincon, C. Tinsley, K. Tinsley, M. Pundik, S. Rojas, A.F. Arrieta, Stiffening multistable origami-inspired deployable structures from embeddable bistable units, Mater. Des. 253 (2025) 113887, https://doi.org/10.1016/j.matdes.2025.113887.
[4] L. Zhang, F. Pan, X. Niu, Y. Wei, L. Yang, Y. Chen, Reprogrammable origami composites with high-loadability, Int. J. Mech. Sci. 305 (2025) 110768, https://doi.org/10.1016/j.ijmecsci.2025.110768.
[5] Y. Li, S. Yu, H. Qing, Y. Hong, Y. Zhao, F. Qi, H. Su, J. Yin, Reprogrammable and reconfigurable mechanical computing metastructures with stable and high-density memory, Sci. Adv. 10 (2024) eado6476, https://doi.org/10.1126/sciadv.ado6476.
[6] H. Pu, L. Mou, S. Yuan, J. Zhu, H. Zhang, J. Luo, Y. Sun, Magnet-based mechanical logic gates With Programmability and continuous operation capability in high-radiation environments, IEEE/ASME Trans. Mechatron. 30 (2025) 7995–8005, https://doi.org/10.1109/TMECH.2025.3554874.
[7] Y. Luo, D.K. Patel, Z. Li, Y. Hu, H. Luo, L. Yao, C. Majidi, Intrinsically multistable soft actuator driven by mixed-mode snap-through instabilities, Adv. Sci. 11 (2024) 2307391, https://doi.org/10.1002/advs.202307391.
[8] X. Cai, B. Tang, S. Li, Venus flytrap-inspired electromagnetically driven bistable gripper for fast envelope grasping, IEEE Robot. Autom. Lett. 10 (2025) 8139–8146, https://doi.org/10.1109/LRA.2025.3583612.
[9] Y. Jiang, X. Tong, J. Li, H. Li, C. Cao, X. Gao, Y. Li, Reprogrammable bistable actuators for multimodal, fast, and ultrasensitive grasping, IEEE/ASME Trans. Mechatron. 29 (2024) 984–994, https://doi.org/10.1109/TMECH.2023.3318976.
[10] J. Li, R. Mu, K. Huo, L. Zhang, H. Zhao, Design and modeling of a self-propagating rotary structures with tunable release mechanism, Int. J. Mech. Sci. 310 (2026) 111079, https://doi.org/10.1016/j.ijmecsci.2025.111079.
[11] S.M. Jo, H.S. Yoon, Energy-efficient tristable soft gripper using shape memory alloy wires for gripping convex and concave objects, J. Mech. Robot. 16 (2024) 021013, https://doi.org/10.1115/1.4062983.
[12] X.S. Liu, B. Yang, Y. Qu, R.A. Liu, Y. Yan, W. Zhang, S.X.A. Zhang, Y.M. Zhang, Multicolor and multistable transparent electrochromic materials and displays, Nat. Commun. 17 (2026) 784, https://doi.org/10.1038/s41467-025-67462-5.
[13] J. Sun, D. Yuan, K. Ju, Y. Xu, Mechanical analysis of multi-stable reconfigurable origami structure, Thin-Walled Struct. 225 (2026) 114762, https://doi.org/10.1016/j.tws.2026.114762.
[14] D. Melancon, A.E. Forte, L.M. Kamp, B. Gorissen, K. Bertoldi, Inflatable origami: multimodal deformation via multistability, Adv. Funct. Mater. 32 (2022) 2201891, https://doi.org/10.1002/adfm.202201891.
[15] Z. Ren, D. Qi, Z. Liu, Z. Qu, Multistable chiral-twist metamaterials with reconfigurable deformation modes: mechanical design, simulations and experimental demonstrations, Thin-Walled Struct. 225 (2026) 114784, https://doi.org/10.1016/j.tws.2026.114784.
[16] Y. Chen, T. Tan, Z. Yan, General-purpose mechanical computing enabled by origami circuit reconfiguration with robotic addressing and activation, Nat. Commun. 16 (2025) 10483, https://doi.org/10.1038/s41467-025-65464-x.
[17] T. Mei, C.Q. Chen, In-memory mechanical computing, Nat. Commun 14 (2023) 5204, https://doi.org/10.1038/s41467-023-40989-1.
[18] T.W. Liu, J.B. Bai, N. Fantuzzi, X. Zhang, Thin-walled deployable composite structures: a review, Prog. Aerosp. Sci. 146 (2024) 100985, https://doi.org/10.1016/j.paerosci.2024.100985.

[19] X. Ma, N. An, Q. Cong, et al., Design, modeling, and manufacturing of high strain composites for space deployable structures, Commun. Eng. 3 (2024) 78, https://doi.org/10.1038/s44172-024-00223-2.
[20] M.J.A.A. Raja, S.A. Hassan, C.Y. Chang, C.M. Shu, A.K. Kiani, M. Shoaib, M.A.Z. Raja, Design of intelligent Bayesian regularized deep cascaded NARX neurostructure for predictive analysis of FitzHugh-Nagumo bioelectrical model in neuronal cell membrane, Biomed. Signal Process. Control. 101 (2025) 107192, https://doi.org/10.1016/j.bspc.2024.107192.
[21] S.A. Hassan, M.J.A.A. Raja, C.Y. Chang, C.M. Shu, M. Shoaib, A.K. Kiani, M.A.Z. Raja, Nonlinear chaotic Lorenz-Lü-Chen fractional order dynamics: a novel machine learning expedition with deep autoregressive exogenous neural networks, Chaos Solitons Fractals 189 (2024) 115620, https://doi.org/10.1016/j.chaos.2024.115620.
[22] R. Chen, X. Jin, S. Laima, Y. Huang, H. Li, Intelligent modeling of nonlinear dynamical systems by machine learning, Int. J. Non-Linear Mech. 142 (2022) 103984, https://doi.org/10.1016/j.ijnonlinmec.2022.103984.
[23] K. Fu, H. Li, P. Deng, Chaotic time series prediction using DTIGNet based on improved temporal-inception and GRU, Chaos Solitons Fractals 159 (2022) 112183, https://doi.org/10.1016/j.chaos.2022.112183.
[24] X. Sun, J. Qian, J. Xu, Compressive-sensing model reconstruction of nonlinear systems with multiple attractors, Int. J. Mech. Sci. 265 (2024) 108905, https://doi.org/10.1016/j.ijmecsci.2023.108905.
[25] Q. Liu, Z. Hou, Y. Zhang, X. Xu, D. Jiang, Some practical regards on the application of the physics-informed sparse identification for strongly NESs, Commun. Nonlinear Sci. Numer. Simul. 143 (2025) 108610, https://doi.org/10.1016/j.cnsns.2025.108610.
[26] L.A. Tavares, P.E.O.G.B. Abreu, L.A. Aguirre, Nonlinearity compensation based on identified NARX polynomials models, Nonlinear Dyn 107 (2022) 709–725, https://doi.org/10.1007/s11071-021-06797-2.
[27] S. Schar, S. Marelli, B. Sudret, Emulating the dynamics of complex systems using autoregressive models on manifolds (mNARX), Mech. Syst. Signal Process. 208 (2024) 110956, https://doi.org/10.1016/j.ymssp.2023.110956.
[28] S. Benftima, S. Gharab, R. Rivas-Perez, V. Feliu-Batlle, Modeling of an irrigation main canal pool based on a NARX-ANN system identification, Commun. Nonlinear Sci. Numer. Simul. 132 (2024) 107929, https://doi.org/10.1016/j.cnsns.2024.107929.
[29] Y.P. Zhu, Z.Q. Lang, Y.Z. Guo, Nonlinear model standardization for the analysis and design of nonlinear systems with multiple equilibria, Nonlinear Dyn 104 (2021) 2553–2571, https://doi.org/10.1007/s11071-021-06429-9.
[30] R. Bolboaca, P. Haller, Enhanced long short-term memory architectures for chaotic systems modeling: An extensive study on the Lorenz system, Chaos 34 (2024) 123152, https://doi.org/10.1063/5.0238619.
[31] A. Ghosh, A. Honore, S. Chatterjee, DANSE: Data-driven non-linear state estimation of model-free process in unsupervised learning setup, IEEE Trans. Signal Process. 72 (2024) 1824–1838, https://doi.org/10.1109/TSP.2024.3383277.
[32] Y. Shang, M. Zheng, Y. Wang, M. Yuan, H. Zhao, Research on deep echo state networks with reservoir interactions, Expert Syst. Appl. 305 (2026) 130861, https://doi.org/10.1016/j.eswa.2025.130861.
[33] R. Zhang, Y. Liu, H. Sun, Physics-informed multi-LSTM networks for metamodeling of nonlinear structures, Comput. Methods Appl. Mech. Eng. 369 (2020) 113226, https://doi.org/10.1016/j.cma.2020.113226.
[34] S.L. Brunton, J.L. Proctor, J.N. Kutz, Discovering governing equations from data by sparse identification of nonlinear dynamical systems, Proc. Natl. Acad. Sci. U.S.A. 113 (2016) 3932–3937, https://doi.org/10.1073/pnas.1517384113.
[35] Y.Tian Z.Huang, C. Li, G. Lin, L. Wu, Y. Wang, H. Jiang, Data-driven automated discovery of variational laws hidden in physical systems, J. Mech. Phys. Solids 137 (2020) 103871, https://doi.org/10.1016/j.jmps.2020.103871.
[36] D.A. Messenger, D.M. Bortz, Weak SINDy, Galerkin-based data-driven model selection, Multiscale Model. Simul. 19 (2021) 1474–1497, https://doi.org/10.1137/20M1343166.
[37] Q. Jiang, C. Yu, Y. Zhou, Z. Zhao, Q. Gao, B. Sun, Modeling and analysis of beam-spring magnetically coupled bistable energy harvester for broadband vibration energy harvesting, J. Sound Vib. 579 (2024) 118373, https://doi.org/10.1016/j.jsv.2024.118373.
[38] T. Wang, Y. Tang, T. Yang, Z.S. Ma, Q. Ding, Bistable enhanced passive absorber based on integration of nonlinear energy sink with acoustic black hole beam, 544(2023) 117409. https://doi.org/10.1016/j.jsv.2022.117409.
[39] J. Mao, W. Gao, C. Liu, D. Cao, S. Lai, Transition analysis of meta-stable and bi-stable nonlinear behavior in piezoelectric vibration energy harvesting through a pre-shaped curved beam model, Appl. Math. Mech. (Engl. Ed.) 46 (2025) 2017–2034, https://doi.org/10.1007/s10483-025-3319-6.
[40] Y. Jin, L. Hou, S. Zhong, H. Yi, Y. Chen, Invertible Koopman Network and its application in data-driven modeling for dynamic systems, Mech. Syst. Signal Process. 200 (2023) 110604, https://doi.org/10.1016/j.ymssp.2023.110604.
[41] Y. Jin, L. Hou, H. Yi, S. Zhong, J. Li, S. Wang, H. Chen, Invertible Koopman network with external inputs: a novel data-driven modeling method for non-autonomous nonlinear systems with discrete spectrum, Neurocomputing 660 (2026) 131869, https://doi.org/10.1016/j.neucom.2025.131869.
[42] Y. Jin, L. Hou, X. Ge, Q. Gao, H. Yi, Z. Li, Y. Feng, S. Zhong, A novel data-driven modeling and efficient model predictive control framework for non-autonomous nonlinear systems based on the Invertible Koopman Network, Nonlinear Dyn 113 (2025) 20605–20631, https://doi.org/10.1007/s11071-025-11277-y.
[43] H. Yasuda, K. Yamaguchi, Y. Miyazawa, R. Wiebe, J.R. Raney, J. Yang, Data-driven prediction and analysis of chaotic origami dynamics, Commun. Phys. 3 (2020) 168, https://doi.org/10.1038/s42005-020-00431-0.
[44] J. Qian, X. Sun, J. Xu, A data-driven reconstruction method for dynamic systems with multistable property, Nonlinear Dyn 111 (2023) 4517–4541, https://doi.org/10.1007/s11071-022-08082-2.
[45] J. Qian, X. Sun, J. Xu, L. Cheng, Discovering differential governing equations of hysteresis dynamic systems by data-driven sparse regression method, Nonlinear Dyn 112 (2024) 12137–12157, https://doi.org/10.1007/s11071-024-09647-z.
[46] J. Qian, X. Sun, L. Cheng, Q. Lv, J. Xu, Time-frequency-domain synergistic reconstruction for multi-stable deployable structure under broadband noise interference, Aerosp. Sci. Technol. 168 (2026) 111268, https://doi.org/10.1016/j.ast.2025.111268.
[47] R. Jin, Q. Liu, Y. Ma, X. Shen, Y. Wang, H. Qian, D. Jiang, Physics-informed harmonic balance identification of high-dimensional structures with nonlinear stiffness and damping, Int. J. Non-Linear Mech. 181 (2026) 105282, https://doi.org/10.1016/j.ijnonlinmec.2025.105282.
[48] R.L. Harne, B.A. Goodpaster, Impedance measures in analysis and characterization of multistable structures subjected to harmonic excitation, Mech. Syst. Signal Process. 98 (2018) 78–90, https://doi.org/10.1016/j.ymssp.2017.04.036.
[49] B. Danish, P.M. Anilkumar, B.N. Rao, Suppression of cross-well vibrations of a bistable square cross-ply laminate using an additional composite strip, Int. J. Dyn. Control. 11 (2023) 2680–2690, https://doi.org/10.1007/s40435-023-01153-1.
[50] H. Mofatteh, B. Shahryari, A. Mirabolghasemi, A. Seyedkanani, R. Shirzadkhani, G. Desharnais, A. Akbarzadeh, Programming multistable metamaterials to discover latent functionalities, Adv. Sci. 9 (2022) 2202883, https://doi.org/10.1002/advs.202202883.
[51] S. Zhu, Y. Wang, Scaled sequential threshold least-squares (S2TLS) algorithm for sparse regression modeling and flight load prediction, Aerosp. Sci. Technol. 85 (2019) 514–528, https://doi.org/10.1016/j.ast.2018.12.038.
[52] A. Chandra, B. Daniels, M. Curti, K. Tiels, E.A. Lomonova, D.M. Tartakovsky, Discovery of sparse hysteresis models for piezoelectric materials, Appl. Phys. Lett. 122 (2023) 214101, https://doi.org/10.1063/5.0146134.
[53] H. Chen, Y. Zeng, H. Ding, S. Lai, L. Chen, Dynamics and vibration reduction performance of asymmetric tristable nonlinear energy sink, Appl. Math. Mech. (Engl. Ed.) 45 (2024) 389–406, https://doi.org/10.1007/s10483-024-3095-9.
[54] H. Han, V. Sorokin, L. Tang, D. Cao, Lightweight origami isolators with deployable mechanism and quasi-zero-stiffness property, Aerosp. Sci. Technol. 121 (2022) 107319, https://doi.org/10.1016/j.ast.2021.107319.
[55] T. Zhao, X. Dang, K. Manos, S. Zang, J. Mandal, M. Chen, G.H. Paulino, Modular chiral origami metamaterials, Nature 640 (2025) 931–940, https://doi.org/10.1038/s41586-025-08851-0.